ETH
Eidgenössische Technische Hochschule Zürich
Swiss Federal Institute of Technology Zurich

IPA

ETH ZÜRICH

MASTER THESIS

Study of the stitching region and η-correction of novel passive CMOS sensors for the HL-LHC upgrade of the CMS pixel detector

Author:
David Lukas BACHER

Supervisors:
Prof. Dr. Rainer WALLNY
Dr. Malte BACKHAUS

CERN-THESIS-2022-117
11/04/2022

11th April, 2022

Abstract

Study of the stitching region and η-correction of novel passive CMOS sensors for the HL-LHC upgrade of the CMS pixel detector

Passive CMOS silicon pixel sensors are a novel sensor type for pixel detectors in HEP and are currently a candidate for the Phase-II upgrade of the CMS detector. Passive CMOS sensors produced in a commercial 150 nm CMOS process use stitching for the production of large scale sensors. A study of the impact of stitching on the performance of unirradiated sensors is presented in this thesis. Testbeam data with 120 GeV pions has been analysed and the measured cluster size, collected charge, diffused charge and detection efficiency in pixels with stitching has been compared to pixels without stitching. No difference between pixels with and without stitching was measured and no influence of the stitching on sensor performance could be observed. An additional study of the sensor resolution for two pixel clusters has been performed. Non-linear charge division worsens the spatial resolution of pixel detectors. The η-algorithm is able to efficiently correct for this effect. The impact of this algorithm on the resolution of two pixel clusters for passive CMOS sensors has been investigated. The η-correction significantly improves the spatial resolution by a factor of two for angles below 4°. No improvement is seen anymore for 9° as expected for the pixel dimensions.

ETH

Eidgenössische Technische Hochschule Zürich
Swiss Federal Institute of Technology Zurich

Declaration of originality

The signed declaration of originality is a component of every semester paper, Bachelor's thesis, Master's thesis and any other degree paper undertaken during the course of studies, including the respective electronic versions.

Lecturers may also require a declaration of originality for other written papers compiled for their courses.

I hereby confirm that I am the sole author of the written work here enclosed and that I have compiled it in my own words. Parts excepted are corrections of form and content by the supervisor.

Title of work (in block letters):

Study of the stitching region and η-correction of novel passive CMOS sensors for the HL-LHC upgrade of the CMS pixel detector

Authored by (in block letters):

For papers written by groups the names of all authors are required.

Name(s):	**First name(s):**
Bacher	David

With my signature I confirm that

- I have committed none of the forms of plagiarism described in the 'Citation etiquette' information sheet.
- I have documented all methods, data and processes truthfully.
- I have not manipulated any data.
- I have mentioned all persons who were significant facilitators of the work.

I am aware that the work may be screened electronically for plagiarism.

Place, date	**Signature(s)**
Zürich, 11.04.2022	D. Bacher

For papers written by groups the names of all authors are required. Their signatures collectively guarantee the entire content of the written paper.

Acknowledgements

I would like to express my sincere thanks to Prof. Dr. Rainer Wallny and Dr. Malte Backhaus for the opportunity to perform this Master thesis in the CMS pixel group at ETH Zürich. Secondly, I want to specially thank Franz Glessgen for his great support throughout this thesis and the many fuitful discussions during this time. I want to thank Dr. Branislav Ristic for the great organisation and supervision during the two weeks of testbeam at CERN and his support during the analysis afterwards. I also want to thank my sister-in-law Stefanie Kolberg for spell and grammar checking this work. Finally but most importantly, I want to thank my family for always supporting me with their biggest dedication in and outside of my studies and this thesis.

To my family

Contents

Chapter 1

Introduction

The Large Hadron Collider (LHC) is currently the largest particle accelerator in the world. From 2026 until the end of 2028 it will undergo construction for the upgrade to the High-Luminosity LHC which will drastically improve its performance. The instantaneous luminosity is planned to be increased by a factor of five. During the time of the upgrade, the Compact Muon Solenoid (CMS) experiment will also need to be upgraded in order to withstand the increased radiation dose and pile-up resulting from the improved luminosity. A crucial part of the CMS detector that needs to be upgraded is the pixel detector. It is the detector part which is located closest to the interaction point and thus receives the highest radation dose and highest particle fluence. The goals of the upgrade are an increased radiation hardness, increased readout speed and increased spatial resolution.

For this upgrade, University of Bonn, ETH Zürich and University of Zürich have developed and tested novel passive CMOS pixel sensors. They are produced in a commercial 150 nm CMOS process, which uses a lithographic production technique called stitching. With this technique, the sensor is not produced as a whole at once but it is divided into indivdual parts which are produced and aligned step-by-step. This allows for the production of larger sensor sizes at smaller costs in commercial foundries and for more design possibilities by using a 150 nm CMOS process. The region on the sensor, where two parts are aligned and connected together is called a stitching line. For the application of passive CMOS sensors in high energy physics and the upgrade of the CMS detector, the performance of the sensor should not be influenced by the stitching line. The goal of part of this thesis is to investigate the impact of stitching on the perfomance of passive CMOS sensors. Specifically, the cluster size, collected charge, charge diffusion and detection efficiency will be measured on the stitching line in a testbeam analysis and compared to regions on the sensor without stitching.

The second part of this thesis investigates the influence of the application of the η-correction on the resolution of the passive CMOS sensors for two pixel clusters along the short side of the pixels. Non-linear charge division in pixel detectors worsens the spatial resolution for two-pixel clusters when using the charge weighted mean to compute the cluster positions. The η-algorithm uses the integral of the η-distribution to compute the cluster position. This algorithm is in principle able to reconstruct the cluster positions more precisely. Two different implementations of the η-correction will be presented and compared to the uncorrected cluster positions.

A brief introduction to the LHC and CMS and their past and future upgrades is given in chapter 2. In chapter 3 an overview on the working principle and techniques of semiconductor sensors and readout chips is given. Afterwards, chapter 4 gives a

more detailed overview on CMOS processes in high energy physics, and presents the RD53A readout chip with the data acquisition software Phase2-ACF and the passive CMOS pixel sensor project. The testbeam setup and data acquisition and reconstruction is presented in chapter 5. Finally, the results of the measurements and the impact of stitching on sensor performance are presented in chapter 6 and the results for the study of impact of the η-correction are shown in chapter 7.

Chapter 2

LHC and CMS

2.1 The Large Hadron Collider

In this section the Large Hadron Collider (LHC) at CERN in Geneva will be described. After a short non-technical overview, the past upgrades of LHC and the future upgrade towards the High-Luminosity LHC (HL-LHC) will briefly be discussed. The information for this section was in most parts taken from the technical design reports [1], [2], [3], [4] and [5].

2.1.1 Overview

The LHC is the world's largest particle accelerator operating at the highest center of mass (c.o.m.) energy. Four large experiments (ATLAS [6], CMS [7], LHCb [8] and ALICE [9]) and a number of smaller experiments are operating at LHC. Since its commissioning in 2010, a number of relevant observations and discoveries have been made, including the discovery of the Higgs boson by ATLAS and CMS in 2012 [10, 11] and hints of a violation of lepton flavour universality by LHCb in 2021 [12].

The LHC is able to produce proton-proton (pp), lead-lead (PbPb) and proton-lead (pPb) collisions. The protons are injected into LHC through a network of smaller accelerators shown in Figure 2.1. Until the end of 2018, H^- ions were, in a first step, accelerated to an energy of 50 MeV in the linear accelerator LINAC2. Then the ions were stripped off of their electrons to produce protons and were then injected into the Proton Synchroton Booster (PSB), where they were further accelerated to 1.4 GeV. Since 2020, LINAC2 has been replaced by the new linear accelerator LINAC4, which accelerates the H^- ions to an energy of 160 MeV. PSB then accelerates the stripped protons from LINAC4 to an energy of 2 GeV [13]. From PSB the protons are injected into the Proton Synchrotron (PS) where their energy will be increased to 25 GeV. From PS the protons are further injected into the Super Proton Synchrotron (SPS) where they will reach an energy of 450 GeV before being injected into LHC where they will be accelerated to their final energy of 6.8 TeV.

In the most recent data taking period from 2015 to 2018, LHC has been operating at a c.o.m. energy of $\sqrt{s} = 13\,\text{TeV}$ and a bunch spacing (time between individual proton bunches) of 25 ns, reaching a peak instantaneous luminosity of $\mathcal{L} = 2 \times 10^{34}\,\text{cm}^{-2}\,\text{s}^{-1}$ and a mean number of proton-proton (pp) collisions per bunch crossing (pile-up) of 53. Since 2010, the LHC has delivered an integrated luminosity of almost $200\,\text{fb}^{-1}$. The yearly increase in integrated luminosity for the ATLAS and CMS experiments is shown in Figure 2.2.

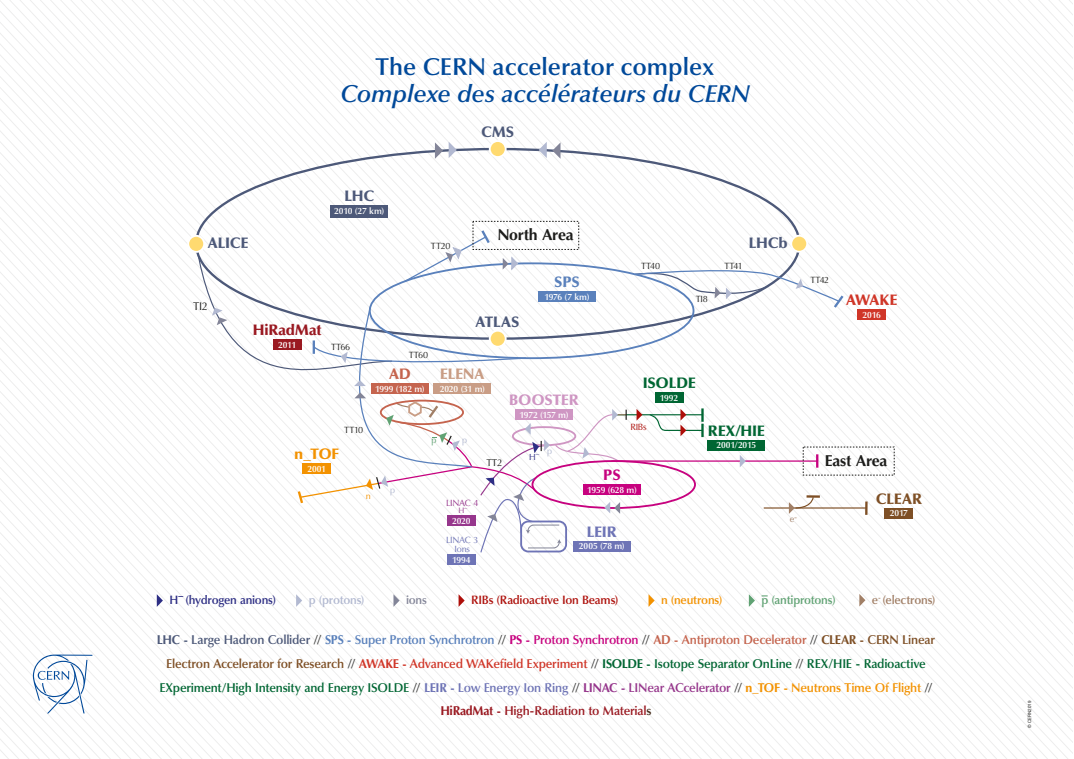

FIGURE 2.1: The CERN accelerator complex. Protons are injected into LHC through LINAC4, PSBooster, PS and SPS. Figure reproduced from [14].

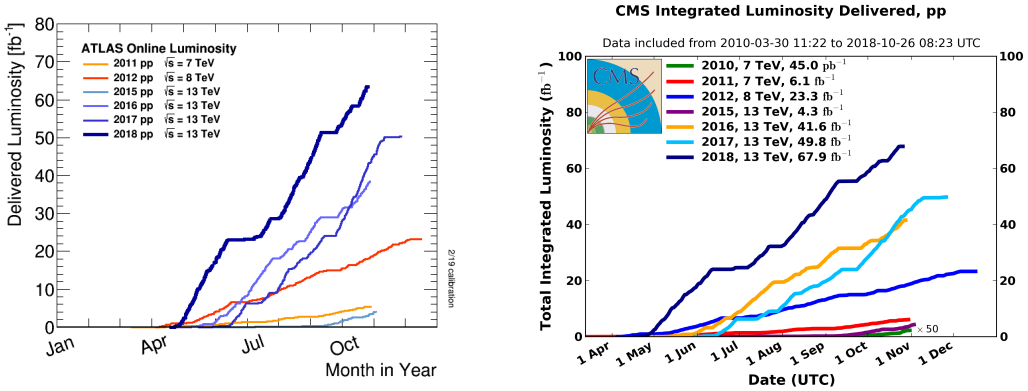

FIGURE 2.2: Yearly integrated luminosity for ATLAS (left) end CMS (right).The plots are taken from [15] and [16] respectively.

2.1.2 Past upgrades of the LHC

The initial design goals of LHC were to reach a peak instantaneous luminosity of $\mathcal{L} = 1 \times 10^{34}\,\mathrm{cm}^{-2}\,\mathrm{s}^{-1}$ at an energy of $\sqrt{s} = 14\,\mathrm{TeV}$ with a 25 ns bunch spacing and 1.15×10^{11} protons per bunch.

At the start of the first data-taking period (Run-1) from 2010 to 2012 LHC operated at a c.o.m. energy of $\sqrt{s} = 7\,\mathrm{TeV}$ with a bunch spacing of 50 ns reaching an instantenous luminosity of $\mathcal{L} = 2.1 \times 10^{32}\,\mathrm{cm}^{-2}\,\mathrm{s}^{-1}$ and collecting a total integrated luminosity of $6.1\,\mathrm{fb}^{-1}$ [3]. In 2012 the c.o.m. energy was increased to $\sqrt{s} = 8\,\mathrm{TeV}$ and the instantanous luminosity to $7.7 \times 10^{33}\,\mathrm{cm}^{-2}\,\mathrm{s}^{-1}$ and an integrated luminosity of $23.3\,\mathrm{fb}^{-1}$ was delivered [3].

After each data-taking period LHC enters a longer shutdown period, referred to as Long Shutdowns (LS), to upgrade and consolidate the accelerator and experiments in order to achieve the goals of the initial design and beyond. During the first long shutdown (LS1), from 2013 to 2014, the c.o.m. energy was further increased to $\sqrt{s} = 13\,\mathrm{TeV}$ and the bunch spacing was reduced to the design goal of 25 ns [1]. During the subsequent Run-2 data taking period from 2015 to 2018, the instantenous luminosity was continously increased reaching a peak value in 2018 of $\mathcal{L} = 2 \times 10^{34}\,\mathrm{cm}^{-2}\,\mathrm{s}^{-1}$, twice the design goal, and a total integrated luminosity of $160\,\mathrm{fb}^{-1}$ was delivered to the ATLAS and CMS experiments [1].

In the second Long Shutdown (LS2), which lasted from 2019 until the end of 2021, the injector chain was further improved in order to achieve larger bunch populations for the operation in Run-3 from 2022 to 2025. It is planned to reach a bunch population of 1.4×10^{11} in 2022 and 1.8×10^{11} from 2023 onwards [4]. The c.o.m energy will be increased to 13.6 TeV, almost reaching the design goal of 14 TeV, and an integrated luminosity of $250\,\mathrm{fb}^{-1}$ is targeted for Run-3 [17]. At the end of Run-3, LHC will have delivered an integrated luminsoity of almost $450\,\mathrm{fb}^{-1}$, well above the initial goal of $300\,\mathrm{fb}^{-1}$ [1].

2.1.3 The High-Luminosity LHC

After the end of Run-3, LHC will go into its third Long Shutdown (LS3) from 2026 until the end of 2028. During LS3, the accelerator will be upgraded to the High-Luminosity LHC (HL-LHC), which will be able to deliver peak instantaneous luminosities of up to $7.5 \times 10^{34}\,\mathrm{cm}^{-2}\,\mathrm{s}^{-1}$ increasing the average pile-up by a factor of 4 to reach 200 [1]. This level of luminosity should enable a collection of $300\,\mathrm{fb}^{-1}$ to $400\,\mathrm{fb}^{-1}$ per year [1]. In its lifetime, the HL-LHC could yield an ultimate total integrated luminosity of $4000\,\mathrm{fb}^{-1}$ [1].

The luminosity increase of the HL-LHC will be achieved by improving the injection chain, specifically by the replacement of the focusing quadrupoles and the use of crab cavities in front of the interaction points, eliminating the luminosity reduction from crossing angle effects [1].

2.2 The Compact Muon Solenoid

In this section an overview of the Compact Muon Solenoid (CMS) detector and its individual components is presented. Then a brief overview of the requirements and planned upgrades for operation at the HL-LHC (Phase-II upgrade) is given and the Phase-II upgrade of the pixel detector is described in more details. The information

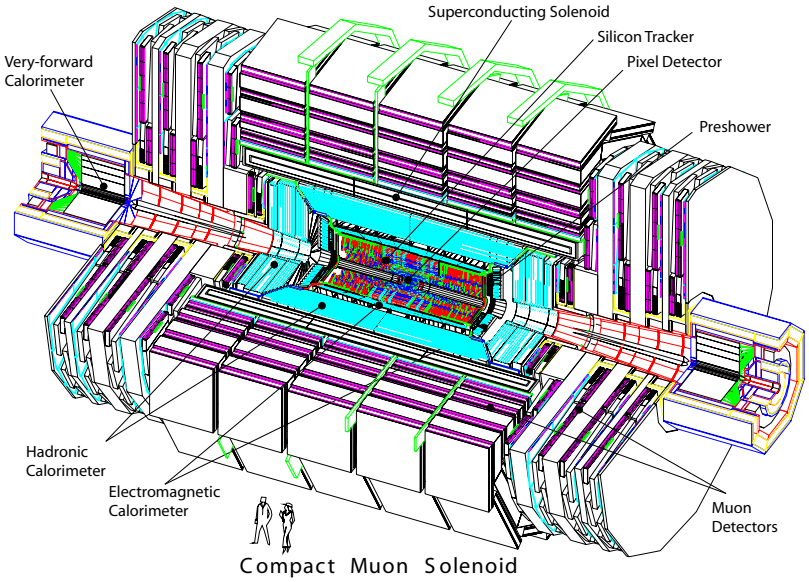

FIGURE 2.3: An exploded view of the CMS detector. Plot reproduced from [19]

for this section is taken from [7], [2], [3] and [18]. For a description of the coordinate system used by CMS, see Appendix A.

2.2.1 Overview

The CMS experiment is a general purpose detector at the LHC at CERN in Geneva. The goal of CMS is to explore the standard model and possibilities of new physics at the highest currently achievable energies. One objective was the discovery of the Higgs boson in 2012 [11]. Other objectives include searches for supersymmetric particles, dark sectors and extra dimensions. In order to achieve these goals, a set of requirements for the CMS detector have been set [7]:

- Good muon identification and momentum resolution over a wide range of momenta and angles, good dimuon mass resolution ($\approx 1\,\%$ at 100 GeV), and the ability to determine unambiguously the charge of muons with $p < 1$ TeV;
- Good charged-particle momentum resolution and reconstruction efficiency in the inner tracker. Efficient triggering and offline tagging of τ's and b-jets, requiring pixel detectors close to the interaction region;
- Good electromagnetic energy resolution, good invariant mass resolution for diphoton and dielectron events ($\approx 1\,\%$ at 100 GeV), wide geometric coverage, π^0 rejection, and efficient photon and lepton isolation at high luminosities;
- Good missing-transverse-energy and dijet-mass resolution, requiring hadron calorimeters with a large hermetic geometric coverage and with fine lateral segmentation.

To meet these requirements, the main features of CMS are a high-field solenoid, a full-silicon-based inner tracking system, and a homogenous scintillating-crystals-based electromagnetic calorimeter. An overview of the CMS detector is shown in Figure 2.3. The individual components of the CMS detector will be briefly described below [7]:

Tracker

The purpose of the tracker is the tracking of trajectories of charged particles in order to provide a good momentum resolution and secondary vertex detection. The CMS tracker is divided into two regions, the inner tracker and the outer tracker. The inner tracker originally consisted of three layers of silicon pixel detectors in the barrel region, which was upgraded to four layers during the Phase-I upgrade in 2016, and two layers in the forward regions (upgraded to three layers). The pixel detectors have pixel sizes of 100 µm $\times$ 150 µm with a thickness of 300 µm and are placed closest to the interaction point with distances in r between 29 mm and 160 mm in the barrel and up to 500 mm in the endcaps [18]. The outer tracker consists of ten layers in the barrel and twelve layers in the forward regions of silicon microstrip detectors with strip pitches between 80 µm and 183 µm and thicknesses of 320 µm to 500 µm. The microstrips are placed at radii between 20 cm and 160 cm in the barrel and distances of up to 113 cm in the endcaps.

The tracker needs to provide a good granularity in order to achieve a good momentum resolution of charged particles and needs to be sufficiently radiation hard as it will see the highest particle flux due to its close placement to the interaction point.

Electromagnetic calorimeter (ECAL)

The electromagnetic calorimeter (ECAL) surrounds the tracker and is used to measure the energy of electrons and photons produced in the collisions. The ECAL consists of lead tungstate ($PbWO_4$) scintillating crystals. It is made of 61 200 crystals in the barrel region ($|\eta| < 3$) and 7324 crystals in the two endcaps. In front of the endcaps a preshower detector is installed for a better π^0 rejection. The scintillation light is collected by silicon avalanche photodiodes (APDs) in the barrel and vacuum photo triodes (VPTs) in the endcap region. Because of their high density, short radiaton length and fast scintillation decay time, $PbWO_4$ crystals allow for a fast, fine granularity and compact calorimeter. In the barrel, the ECAL has a thickness of 230 mm corresponding to 25.8 X_0, in the endcaps the thickness is 220 mm corresponding to 24.7 X_0.

Hadronic calorimter (HCAL)

The hadronic calorimeter (HCAL) is placed outside of the ECAL and is used to measure the energy of hadrons by producing and detecting hadronic showers. In the barrel region ($|\eta| < 3$), it consists of 14 brass plates and two steel plates as the innermost and outermost layers, acting as absorbers. The absorbers are alternated with layers of plastic scintillators, which will detect the hadronic showers produced in the absorbers. The scintillation light is converted by wavelength-shifting (WLS) fibres and collected by hybrid photodiodes (HPDs). The HCAL in the barrel region is complemented by a tail catcher outside of the solenoid, ensuring a thickness of at least 11 hadronic interaction lengths. In the endcaps, a Cerenkov based iron/quartz-fibre calorimeter is used.

Superconducting magnet

Outside of the HCAL a 13 m long superconducting magnet with 6 m inner diameter provides a 4 T magnetic field. The purpose of the field is to bend the tracks of

charged particles inside and outside of the solenoid for a good momentum resolution of these particles. On the inside, the solenoid houses the tracker, ECAL and HCAL. On the outside, the return field is strong enough to saturate 1.5 m iron yokes.

Muon system

Outside of the solenoid, four muon stations are integrated into the iron return yoke. These muon stations serve for the identification of muons, momentum measurement and triggering. A powerful muon detection is of central importance for recognizing interesting signatures over a large background. Each muon station consists of layers of aluminium drift tubes (DT) in the barrel region and cathode strip chambers (CSC) in the endcaps. Additionally, the barrel and endcap are complemented by resistive plate chambers (RPC), which provide a dedicated trigger system with a sharp p_T threshold.

Trigger

The bunch spacing of LHC is 25 ns, which equals a crossing frequency of 40 MHz. In Run-2, the average pile-up was 53. This produces an amount of data which is impossible to fully store and process. The amount of data is reduced by a trigger system selecting which events to store, depending on predefined event characteristics. The process happens in two steps called Level-1 (L1) Trigger and High-Level Trigger (HLT). The L1 Trigger is hardware based and consists of custom-designed electronics, while the HLT is software based. The design output rate of the L1 Trigger is 100 kHz. Together with the HLT, the output data is reduced by a factor of 10^6.

2.2.2 The CMS Phase-II upgrade

The CMS detector needs to be upgraded during LS3 in order to withstand the increased luminosity and particle flux provided by the HL-LHC. This upgrade is called the Phase-II Upgrade. The larger pile-up of up to 200 leads to increased radiation and particle density. This requires an increased radiation hardness of the detector components as well as increased detector granularity and increased bandwidth and trigger rates for the higher data rates.

The trigger system will be upgraded to allow for a maximum L1 Trigger rate of 750 kHz and 7.5 kHz at the HLT [2]. In the muon systems, the full front-end electronics for the DTs and CSCs will be replaced to increase radiation tolerance and in the forward region improved RPCs and new gas electron multiplier (GEM) based chambers will be installed [2]. The $PbWO_4$ crystals of the ECAL will be cooled to lower temperatures and the front-end electronics will be replaced in order to be compliant with the new L1 Trigger system and to allow for single crystal information for the L1 trigger [2]. In the HCAL, the HPDs to read out the scintillation light from the plastic scintillator will be replaced with silicon photomultipliers (SiPMs) before LS3 already and the scintillator tiles closest to the beam will be replaced during LS3 [2]. The endcaps of the ECAL and HCAL will be replaced with a combined multi-layer electromagnetic and hadronic calorimeter based on silicon pad sensors to provide higher granularity for improved pile-up rejection and particle identification [2]. The entire tracker will be replaced with the new tracker, providing increased forward acceptance, higher radiation hardness and higher granularity [2].

The new tracker will also be compatible with and provide tracking information to the upgraded L1 trigger. This means that the track has to send out self-selected tracking information at every bunch crossing, which is a main driving factor for the design of the Outer Tracker [3]. This is achieved by modules which are able to reject signals below a certain p_T threshold [3]. The use of tracking information in the L1 trigger will improve the transverse momentum resolution at L1, as well as the usage of information on track isolation and will contribute to the mitigation of pile-up [3].

A more detailed description of the Phase-II Upgrade of the Pixel detector will be given in section 2.2.3.

2.2.3 The Phase-II upgrade of the CMS pixel detector

In order to withstand and exploit the increased radiation and particle density caused by the increased luminosity from HL-LHC, the pixel detector of CMS will have to be replaced during the Phase-II upgrade. The upgraded pixel detector must be able to withstand an integrated luminosity of $3000\,\mathrm{fb}^{-1}$ [20] with little efficiency loss. This integrated luminosity is equivalent to a radiation exposure of up to 2.3×10^{16} $1\,\mathrm{MeV\,n_{eq}\,cm^{-2}}$ [20] for the innermost layers of the pixel detector. In addition, the upgraded detector has to have a higher granularity to keep the pixel occupancy below the per mille level for the increased pile-up of up to 200 [3]. Also a two track separation of the pixel detector will have to be improved to increase the track finding performance in highly energetic jets [3].

The upgraded pixel detector will employ thin n-in-p type silicon sensors of thickness 150 µm and pixel sizes of 25 µm × 100 µm or 50 µm × 50 µm, which are able to withstand the expected radiation dose and deliver the desired levels of resolution and occupancy [3]. For the innermost layer, 3D silicon sensors are also considered. The readout chip will be based on 65 nm CMOS technology and was developed in a joint R&D programme together with the ATLAS collaboration called RD53A [3]. This readout chip will have a total active area of 16.4 mm × 22.0 mm [3]. The RD53A programme and readout chip will be described in more detail in section 4.2.

The layout of the Phase-II pixel detector is shown in Figure 2.4. It consists of four cylindrical layers in the barrel region and twelve disc-like structures in the forward regions which extend the acceptance to $|\eta| \approx 4$ [3]. Modules with two readout chips and four readout chips, arranged as 2×1 and 2×2 respectively, are planned [3]. The pixel detector will be cooled to a temperature of $-20\,^{\circ}\mathrm{C}$ to reduce the noise level in the sensors and readout chips [3].

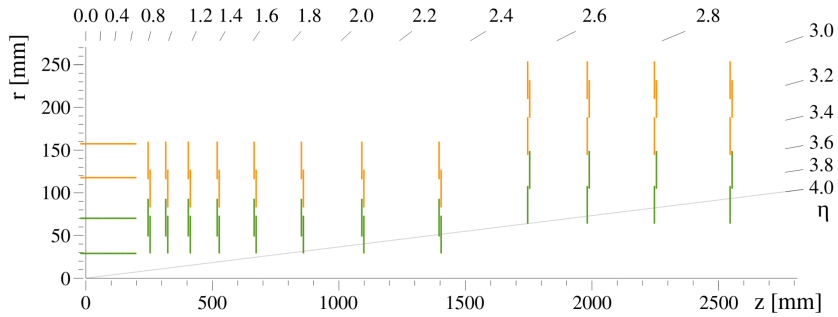

FIGURE 2.4: Sketch of one quarter of the pixel detector layout in r-z view. Green lines correspond to pixel modules made from two readout chips, yellow lines to pixel modules with four readout chips. Figure reproduced from [3].

Chapter 3

The Physics of Pixel Detectors

In this chapter, an overview of the physical and technical working principles of the sensor and readout chip of a hybrid pixel detector will be given. In section 3.1 the energy deposition and charge generation mechanisms in silicon for charged particles will be described. Then in sections 3.2, 3.3 and 3.4 the principle and structure of the sensor and the readout electronics of a hybrid pixel detector will be presented.

3.1 Interaction of charged particles in silicon

The principle of detection of particles and radiation relies on their interactions with the detector material. Part of their energy is deposited in the material, which generates secondary particles which can be detected as electric signals. Typically, semiconductors, and in particular silicon, are used for pixel detectors.

The charge transport in silicon can be described by the band model. While atoms have discrete energy levels, in crystals they become energy bands. The last band that is filled with electrons is called the valence band. The bands with higher energy are called conduction band and contribute to the charge transport in the crystal. Depending on the band gap betewen valence and conduction band, a crystal is either an insulator, a semiconductor or a conductor (see Figure 3.1). In a semiconductor the band gap is small enough (1.12 eV for silicon) that a small fraction of the electrons in the valence band can be thermally excited to the conduction band. Energetic particles interacting with the silicon are able to excite electrons from the valence band to the conduction band, creating electron-hole pairs which can then be measured as an electric current.

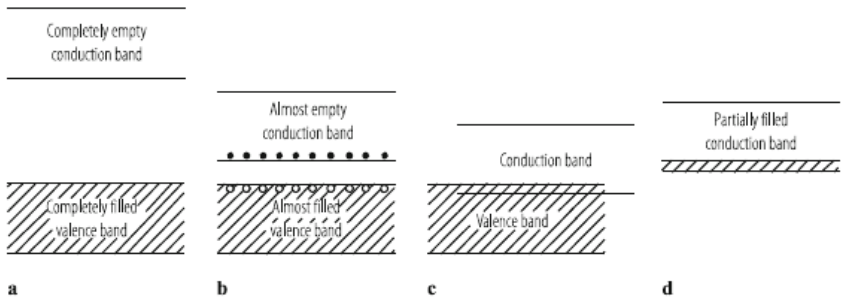

FIGURE 3.1: Energy band structure of insulators (a), semiconductors (b) and conductors (c, d). Figure reproduced from [21].

Charged particles, heavier than the electron, mainly interact with silicon via ionization. Charged particles continously deposit part of their energy via scattering on electrons while passing though the detector material. The mean energy loss per unit path length (stopping power) for charged particles heavier than the electron, is described by the Bethe-Bloch formula which is valid in the region $0.1 \lesssim \beta\gamma \lesssim 1000$ [22]:

$$\left\langle -\frac{dE}{dx} \right\rangle = Kz^2 \frac{Z}{A} \frac{1}{\beta^2} \left[\frac{1}{2} \ln \frac{2m_e c^2 \beta^2 \gamma^2 W_{max}}{I^2} - \beta^2 - \frac{\delta(\beta\gamma)}{2} \right], \tag{3.1}$$

where

$$W_{max} = \frac{2m_e c^2 \beta^2 \gamma^2}{1 + 2\gamma m_e / M + (m_e/M)^2} \tag{3.2}$$

is the maximum possible energy transfer in a single collision and

$\frac{dE}{dx}$: stopping power

$K =$ $4\pi N_A r_e^2 m_e c^2 = 0.307\,075\,\mathrm{MeV\,mol^{-1}\,cm^2}$]

z: charge number of incident particle

Z: atomic number of absorber (14 for silicon)

A: atomic mass of absorber ($28\,\mathrm{g\,mol^{-1}}$ for silicon)

β: velocity of the particle $\beta = \frac{v}{c}$

$m_e c^2$: electron mass $\times c^2$ (0.511 MeV)

γ: Lorentz factor $\frac{1}{\sqrt{1-\beta^2}}$

I: mean excitation energy (173 eV in silicon [23])

$\delta(\beta\gamma)$: density effect correction at high energies

M: incident particle mass.

For low energies ($0.1 \lesssim \beta\gamma \lesssim 1$), the stopping power decreases as $\sim 1/\beta^2$ reaching a minimum at around $\beta\gamma \approx 3$. A particle with minimum stopping power is called minimum ionizing particle (MIP). The minimum stopping power of muons is $1.66\,\mathrm{MeV\,g^{-1}\,cm^2}$ for $\gamma = 3.58$ [22]. For higher energies it increases logarithmically and corrections such as the density effect correction are introduced. For $\beta\gamma \gtrsim 1000$ radiative losses have to be included (see [22] for more information on density-effect corrections and radiative losses).

As can be seen from Equation 3.1 and Equation 3.2, the mean stopping power only has a minor dependence, and only at high energies, on the incident particle's mass M through the maximum energy transfer W_{max}. For most practical purposes, the mean stopping power $\langle dE/dx \rangle$ in a given material is only dependent on β. A plot of the mean stopping power for muons in copper is shown in Figure 3.2.

For thin detectors, the energy loss is subject to significant statistical fluctutations and its distribution is heavily skewed towards larger energy losses. The distribution of the energy loss in thin detectors is described by a Landau distribution. The main reason for these large statistical fluctions are so-called δ-electrons. These are secondary electrons, that obtain enough energy from a single collision with the incident particle to become ionizing particles themselves. The occurence of δ-electrons increases with increasing energies, which increases the mean energy loss for higher energies (Equation 3.1). The maximum or most probable value (mpv) Δ_p of the energy loss

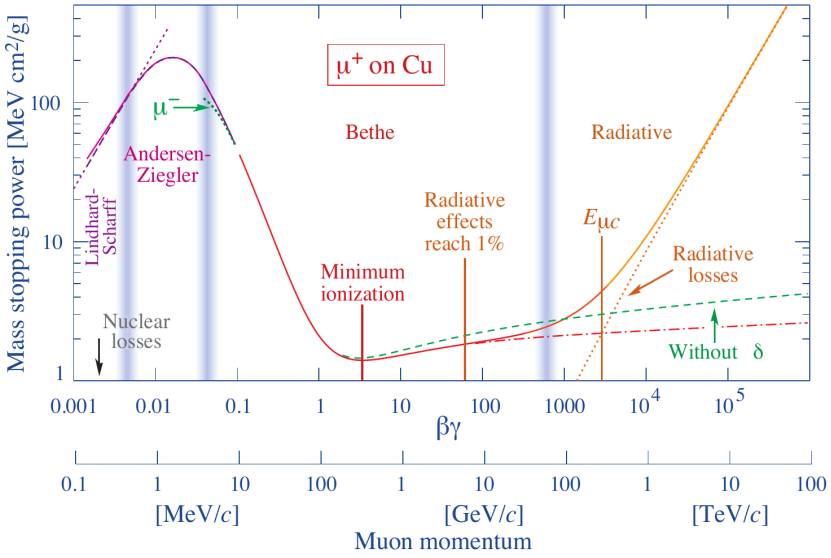

FIGURE 3.2: Mean stopping power for muons in copper as a function of $\beta\gamma$. The region $0.1 \lesssim \beta\gamma \lesssim 1000$ is described by the Bethe-Bloch formula Equation 3.1. For $\beta\gamma \gtrsim 1000$ radiative losses dominate over ionization. For $\beta\gamma \lesssim 0.1$ nuclear losses have to be included. Figure reproduced from [22].

distribution is only minorly affected by the larger tails of the distribution and reaches a plateau for high energies. For this reason, the mpv Δ_p instead of the mean of the distribution is used to describe the energy loss in thin detecors. The mpv energy loss in thin detectors depends on the thickness of the detector and can be calculated as [22]:

$$\Delta_p = \xi \left[\ln \frac{2mc^2\beta^2\gamma^2}{I} + \ln \frac{\xi}{I} + j - \beta^2 - \delta(\beta\gamma) \right], \tag{3.3}$$

where $\xi = (K/2)(Z/A)z^2(x/\beta^2)$ with x the detector thickness in $\mathrm{g\,cm^{-2}}$ and $j = 0.200$. The ratio of the mpv energy loss normalized to the detector thickness and the mean energy loss for the case of muons in silicon for different thicknesses is shown in Figure 3.3.

The δ-electrons deposit their energy across several hundred micrometers inside the silicon. This leads to a shift of the reconstructed hit position of the inital particle and thus limits the resolution of silicon tracking devices.

The number of electron-hole pairs Q generated by a traversing particle is given by

$$Q = \frac{\Delta E}{w} \tag{3.4}$$

where ΔE is the deposited energy of the traversing particle and w is the mean energy needed to create an electron-hole pair. For silicon $w \approx 3.6\,\mathrm{eV}$ [24]. The difference in energy to the band gap of 1.12 eV in silicon generates phonons (lattice vibrations), which will dissipate as thermal energy.

Using the stopping power of MIPs $\frac{dE}{dx}_{min} = 1.66\,\mathrm{MeV\,g^{-1}\,cm^2}$ [22], the density of silicon $\rho_{Si} = 2.33\,\mathrm{g\,cm^{-3}}$ [22] and estimating of the plateau value for the most probable energy loss for a thickness of 150 µm from Figure 3.3 as approximately 0.7, one can

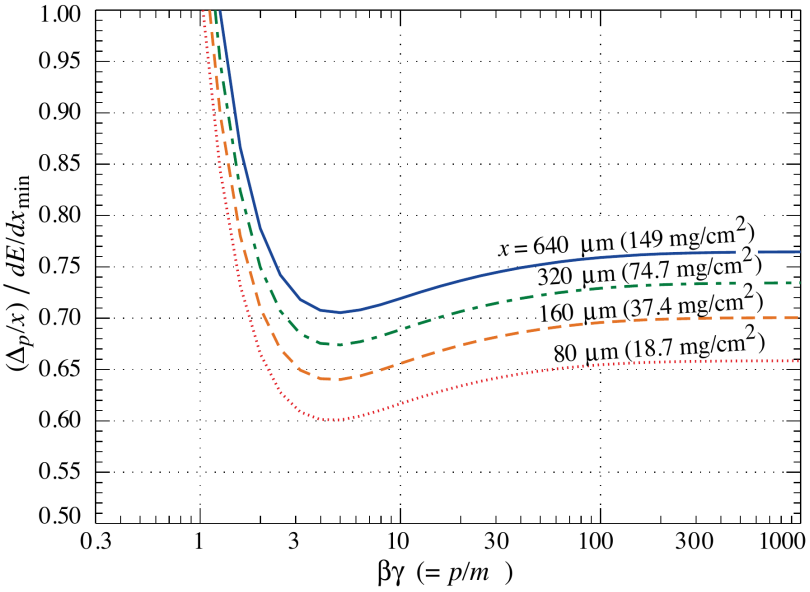

FIGURE 3.3: Most probable energy loss of muons in silicon scaled to the mean loss of a minimum ionizing particle (388 eV µm^{-1} or 1.66 MeV g^{-1} cm^2). Plot reprocuded from [22].

find the number of electron hole pairs generated per unit distance:

$$\frac{1.66\,\mathrm{MeV\,g^{-1}\,cm^2}\cdot 2.33\,\mathrm{g\,cm^{-3}}\cdot 0.7}{3.6\,\mathrm{eV}} = 75\,\mathrm{e^-/\mu m} \tag{3.5}$$

3.2 Hybrid Pixel Detectors

A pixel detector is a device that is able to detect relativistic charged particles and produce images with a high granularity (pixel size). Typically the signal is generated in a semiconductor (e.g. silicon) and processed electronically, with parallel data readout. At high-luminosity conditions, highly specialized sensor material cells individually connected to a dedicated readout chip via small metal bumps (bump bonds) are commonly used. This is called a hybrid pixel detector and a single pixel cell of such a detector is shown in Figure 3.4.

This design has the consequence that the size of the front-end-electronics of a single pixel must match the size of the pixels, which limits its complexity. To deplete the sensor, a sufficiently high voltage has to be applied, which again has to be accounted for in the design of the front-end electroninc s to avoid sparking from large static voltages. Additionally, both the sensor and front-end electronics have to be sufficiently radiation hard in order to withstand the high radiation environment in which they are typically used in high-energy physics applications.

In the next sections, a more detailed overview on the sensor and front-end electronics of a hybrid pixel detector will be given.

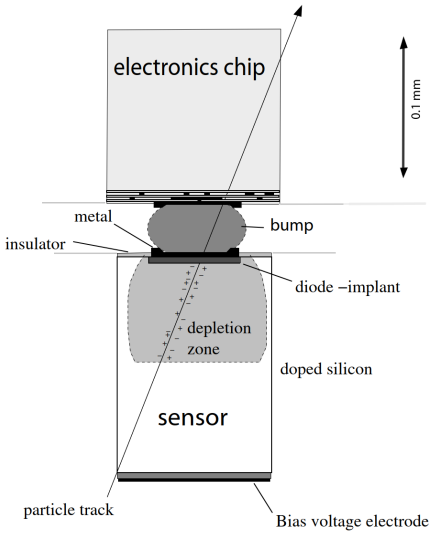

FIGURE 3.4: Schematic view of a single pixel cell. Figure reproduced from [24].

3.3 The Sensor

3.3.1 Silicon Doping

Silicon sensors are made from single crystals, which crystalize in a diamond lattice. Each atom in the crystal is bound with the four closest neighbour atoms, sharing its four valence electrons. For a perfect semiconductor, without any impurities, all valence electrons are bound to their positions at low temperatures. At larger temperatures, thermal excitations (lattice vibrations) can excite an electron and elevate it from the valence band to the conduction band. The free electron in the conduction band and the created hole are thus available for electric conduction. A semiconductor is called intrinsic if the impurity concentration is small compared to the thermally generated free electrons. For silicon the intrinsic charge concentration at room temperture is approximately $10^{10}\,\mathrm{cm}^{-3}$ [21].

By introducing foreign atoms as impurities into the lattice the charge concentration can be changed. This process is called doping. One may introduce atoms with five valence electrons (e.g. P), called donors, or atoms with only three valence electrons (e.g. B), called acceptors. The extra electron of the donors is easily elevated into the conduction band, increasing the concentration of free electrons as charge carriers. These types of doped silicon are called n-doped and have electrons as majority carriers and holes as minority carriers. The missing electron of the acceptors produces a hole, which is able to move as a positive free charge carrier. These types are called p-doped and have holes as majority carriers and electrons as minority carriers.

3.3.2 The pn-junction

The core building block of semiconductor sensors is the pn-junction. When n-doped and p-doped semiconductors are brought together, the majority charge carrriers (electrons in n, holes in p), of one side diffuse into the other side of the junction. There they recombine with the majority charge carriers of the other material leaving behind spatially fixed donor and acceptor ions. This leaves a region close to the junction which is depleted of free charge carriers, called the depletion zone. The

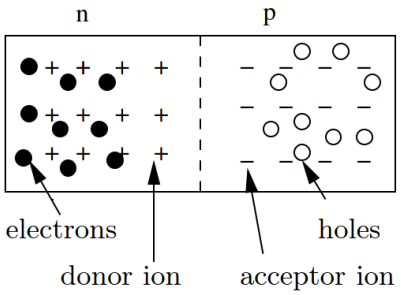

FIGURE 3.5: Schematic illustration of a pn-junction. Figure reproduced from [24].

spatially fixed ions create an electric field which counters the diffusion of the majority charge carriers until a steady state between diffusion and drift due to the electric field is reached. An illsutration of the pn-junction is shown in Figure 3.5.

3.3.3 Reverse Bias

By applying a voltage in the same direction as the internal electric field to the pn-junction, the depletion zone can be increased. The size of the depletion zone can be approximated by [24]

$$W = \sqrt{2\varepsilon_0 \varepsilon_{\mathrm{Si}} \frac{V}{eN}}, \tag{3.6}$$

where N is the dopant concentration, and V the applied voltage. A pn-junction with a voltage applied in this direction is called reversely biased. In a typical sensor a reverse bias is applied such that the depletion zone extends over the full region of the sensor. This is called a fully depleted sensor. This leads to a high electric field in the sensor. The free charges, created either thermally or by a traversing particle, are quickly collected and measurable as a current. The drift velocity of the free charges depends linearly on the applied electric field but saturates at approximately $10^7\,\mathrm{cm\,s^{-1}}$, leading to a fast collection in less then 10 ns [24] and thus a fast response time of the sensor. Thermal excitations in the depletion zone lead to a constant creation of electron-hole pairs, which leads to constant current in the sensor, the so-called leakage current. The leakage current is a source of noise, which can be reduced by cooling the sensor to reduce the rate of thermal excitations.

3.3.4 A typical device

A cross section of a typical device is shown in Figure 3.6. It consists of highly doped p^+-implants placed in a n-bulk silicon wafer. A reverse bias is applied to both sides of the pn-junction until the n-bulk is fully depleted. Charges generated by a traversing particle are quickly collected at the electrodes. Typically the grounded electrode is connected to the readout electronics by a coupling capacitor which will be described in the next section. The spatial resolution is acheived by the segmentation of the p^+-implants in the n-bulk.

3.3.5 Radiation damage

Due to their usage as the innermost tracking detectors in many High-Energy physics experiments, pixel detectors and sensors receive high fluences and radiation rates (up to 1.2 GRad for the Phase-II Upgrade of the CMS pixel detector [20]). This causes

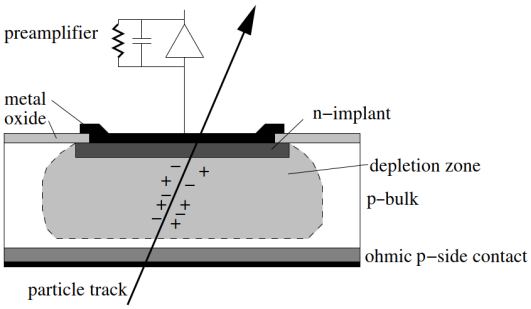

FIGURE 3.6: Schematic cross section of a typical n-in-p device. Figure adapted from [24].

damage to the sensors and electronics, which can usually be divided into two categories: bulk damage and surface damage. The main effects of radiation damage are an increase of the leakage current, change of the space charge and thus an increase of the depletion voltage and charge trapping leading to smaller signals.

Surface damage is caused by ionization in the insulting layers (e.g. the metal oxide layer) which are required for the fabrication. Electrons, which are created by ionizing radiation in these layers, have a high enough mobility to be collected at a nearby electrode. The created holes are trapped, which creates a positive surface charge, which can result in electron accumulation in the silicon at the surface. Additionally, the generation of interface states leads to a surface generation current, which contributes to the leakage current. The effects of surface damage can be controlled by careful design of the sensor [24].

Bulk damage is caused by interaction of the high energetic particles with the silicon nuclei. These interactions can knock the atoms from their lattice positions, resulting in lattice defects. Primary defects are unstable and can either anneal or interact with other defects or impurities and form stable defects in the crystal. The defects can introduce additional energy levels in the band gap, which act as charge traps, or have donor- or acceptor-like behaviours, which leads to a change of the space charge.

3.4 The Front-End Electronics

The signal produced by the sensor needs to be collected and processed for further analysis. For this purpose each pixel sensor is connected to on-chip signal processing cicuitry, called pixel unit cell (PUC), where the information is processed individually and in parallel for each pixel and then tranmitted out together to the data acquisition. A schematic of the typical components of the PUC is shown in Figure 3.7.

3.4.1 Analog Signal Processing

The charge created in the sensor by a traversing particle is fed into the on-chip electronics through the bump pad. There it is first processed by a charge-sensitive amplifier (CSA). The CSA converts the produced charge into a voltage. A simplified circuit of the CSA is shown in Figure 3.8. The CSA consists of an inverting amplifier with gain $-A$ and a feedback capacitance C_f. For an ideal circuit the output voltage

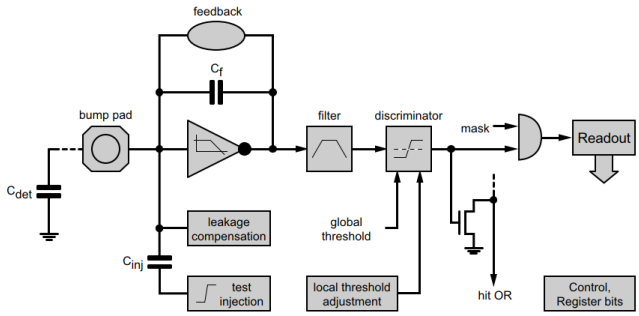

FIGURE 3.7: Schematic of the typical components of the signal processing chain. Figure reproduced from [24].

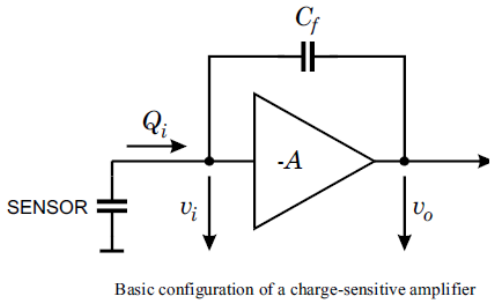

FIGURE 3.8: Simplified charge sensitive amplifier circuit. Figure reproduced from [25].

per input charge is given as [24]:

$$A_q = \frac{v_0}{Q_i} = \frac{-A}{C_f(1+A)}. \tag{3.7}$$

Thus the charge gain can be tuned by the feedback capacitance C_f. The CSA is one of the most crucial parts a in a pixel detector and must provide good amplification of approximately $10^{-4}\,\mathrm{mV/e}$ or equivalently $25\,\mathrm{mV\,MeV^{-1}}$ as well as small power consumption and low noise.

Additionally a feedback circuit is required to remove the charges from the CSA and return the output voltage to its intial value. The discharge of the CSA must be slow enough to allow for further analysis on the output signal but fast enough to avoid saturation and nonlinearities. Chips often use a constant current discharge, which leads to a signal width proportional to the intial charge, which can be used for a "time over threshold" (ToT) analysis.

The output signal of the CSA is compared to a threshold signal by a discriminator. The discriminator outputs a signal, if the CSA output is larger than the threshold. The threshold must be chosen as low a possible in order to maximize the detection efficiency but it needs to be high enough, so that noise hits are still sufficiently rejected. The threshold can be set globally but transistor mismatch, voltage drops and preamplifier gain variations lead to threshold variations between the individual pixels. In order to achieve an uniform threshold distribution among all pixels, local threshold adjustments are performed by digital to analog converters, storing individual trim values for each pixel in digital registers (typically 3-7 bits).

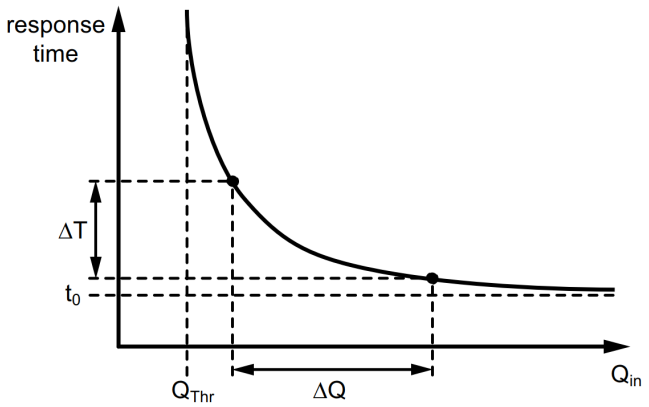

FIGURE 3.9: Response time of a discriminator as a function of the input charge. Figure reproduced from [24].

The precise knowledge of the response time of the discriminator is needed in order to associate an event with a single bunch crossing (25 ns). From the response time curve in Figure 3.9, it can be seen that the response time is much longer for smaller charges. Charges just above the threshold Q_{thresh} take longer to be detected than signal charges. A time window ΔT can be selected on this curve. This defines a window of charges ΔQ which are detected in-time and can be associated to a single bunch crossing. The lowest value in this window is called the in-time threshold.

In order to check the functioning of the signal processing circuitry independently of the sensor and for calibrations of the signal processing, controlled injection of charges is necessary. This is achieved by applying a voltage to a calibration capacitor C_{inj}. In this way, precisely known charges can be injected into the circuitry which can then be used to test and calibrate the detector.

3.4.2 Readout architecture

The digital hit signals of the discriminators must be further processed by the readout architecture. At the LHC, the collisions occur at regular intervals of 25 ns and the bunch crossing clock of LHC can be used to synchronize the data taking. As most events do not contain relevant information, a data selection based on other parts of the CMS detector is made to pick out potentially interesting events. This is called a trigger. The trigger selection at CMS after the Phase-II Upgrade will take 12.5 µs [2] and thus arrives with a delay of several bunch crossings at the pixels. For this reason, the hit information of many events has to be stored on the pixel chip during this latency interval. If a trigger arrives at the pixels, the data is sent out to the data acquisition. If no trigger arrived within the trigger latency the data will be discarded.

Chapter 4

Passive CMOS sensors on the RD53A chip

4.1 CMOS technology in High Energy Physics

Complementary metal-oxide-semiconductors (CMOS) technology uses complementary and symmetrical pairs of p-type and n-type transistors for logic functions. CMOS technology is the most common form of semiconductor device fabrication and is applied in integrated cirucits, microprocessors, microcontrollers, etc., with feature size down to 5 nm. CMOS circuits consume much less power than pure NMOS or PMOS technology, which allows for smaller and higher density appliances.

In high energy physics, CMOS technology has been used for readout chips of silicon detectors since LEP. These early chips used feature size down to 1.5 µm. In 1997, CMOS processes with feature size down to 250 nm were demonstrated to be sufficiently radiation hard to allow for applications in high energy physics [26]. Nowadays basically all silicon detector readout chips are manfactured in CMOS processes. One example is the CMS Phase-I pixel detector readout chip, which uses a 250 nm CMOS process. In section 4.2, the RD53A prototype readout chip for the Phase-II Upgrade of the CMS pixel detector, which employs a 65 nm CMOS process, will be presented.

Additionally, CMOS processes have not only been used for readout chips, but also for the design of monolithic active pixel sensor (MAPS), where the sensor and readout chip are built on the same silicon wafer. This has the advantage that no connection through bump bonds between the sensor and the readout chip is required. For high energy physics applications a high radiation tolerance and fast readout speeds are needed from silicon sensors. The key to these requirements is to establish a depletion zone, where charges created by traversing particles can be collected quickly. The depletion depth d depends on the bias voltage V_B and the bulk resistivity ρ according to

$$w \sim \sqrt{\rho V_B}. \tag{4.1}$$

To achieve sufficient depletion depth at moderate bias voltages, a high bulk resistivity is needed [27]. Classically CMOS technology was only available on low resistivity wavers. With the availability of high-resistivity CMOS processes, advancements were made for fully depleted MAPS. But the technology does not yet offer the logic density comparable to a dedicated readout chip produced in a 65 nm CMOS process, which needed in the Phase-II Upgrade of the CMS pixel detector. Furthermore the current resolution of the CMS pixel detector is mostly limited by the material of the support and cooling structures and would not benefit much from using MAPS.

Min. stable threshold	$600\,e^-$
Min. in-time threshold	$1200\,e^-$
Hit loss from in-pixel pile-up	$\leq 1\,\%$
Trigger rate	1 MHz
Trigger latency	12.5 µs
Noise occupancy per pixel	$< 10^{-6}$

TABLE 4.1: Specifications for the RD53A chip, taken from [30].

A different possibility is to utilize CMOS processes to produce sensors of hybrid pixel detectors. These sensors are called passive CMOS sensors as they do not use any active components. These sensors are able to exploit the possibilities in the production processes of commercial CMOS technology, such as [28]:

- High prouction throughput at low costs.
- Availability of several metal layers which can be used as re-distribution layers.
- Polysilicon layers to connect each pixel to a bias grid which allows for testing the sensor without readout chip.
- Metal-insulator-metal capacitors allowing to AC-couple the pixels with the readout chip preventing leakage currents flowing into the readout channels.

In section 4.4, a more detailed look into passive CMOS sensors produced in a commercial 150 nm CMOS process will presented.

4.2 The RD53A readout chip

The RD53A pixel readout integrated circuit is a prototype readout chip for the Phase-II upgrade of the CMS and ATLAS pixel detectors designed to endure the highly radiative environment of the HL-LHC. It was developed toegether by ATLAS and CMS insitutions in the RD53 collaboration [29]. To be able to achieve the requirements described in section 2.1.3, a set of specifications for the RD53A chip has ben given in [30]. The main goal of the specificatons is an identification rate of 99 % of the incident particle hits. For this a threshold of 600 electrons without any time-walk specification, and an in-time threshold of 1200 electrons should be achieved. Furthermore the noise occupancy should be less than 10^{-6}. Also the readout time must be short enough to allow for the new L1 trigger rate with a latency of 12.5 µs (500 bunch crossings). Table 4.1 summarises these specifications. For the usage of the RD53A chip a manual can be found in [31].

The RD53A chip uses 65 nm CMOS technology and covers an area of 20.0 mm $\times$ 11.6 mm. The general floorplan is shown in Figure 4.1. At the top there is a row of test pads, which are to be removed for the final production. Below there is the pixel matrix of 400×192 pixels of size $50\,\mu m \times 50\,\mu m$. At the bottom is all the global analog and digital circuitry and the wire bond pads. The pixel matrix is built up of 8×8 pixel cores, each divided into 16 analog islands with 4 pixels each. The islands are embeded in an automatically synthesized digital sea. The layout of the islands and the sea is shown in Figure 4.2.

The matrix of the RD53A chip is divided into three different front end designs: Differential, Linear and Synchronous. CMS uses the linear front-end (LFE) for the

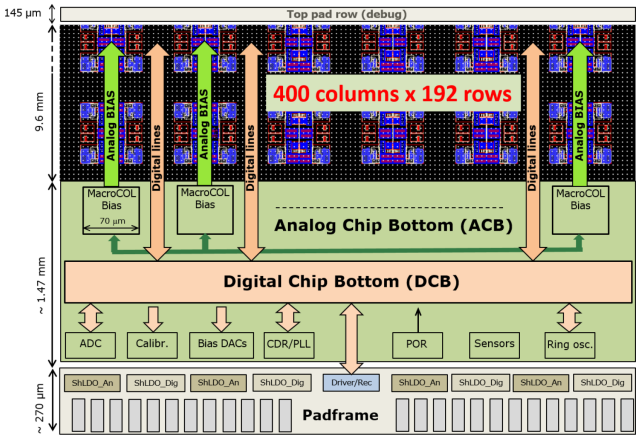

FIGURE 4.1: RD53A floorplan. Figure reproduced from [31].

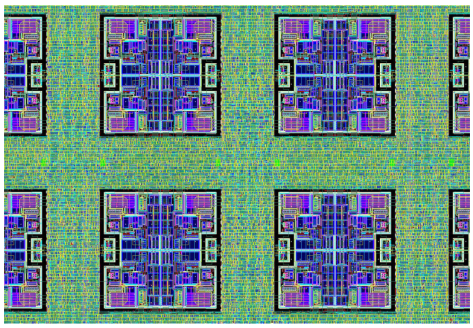

FIGURE 4.2: Layout of the analog islands and the digital sea. Figure reproduced from [31].

Phase-II upgrade, thus the other two designs will not be presented here. The LFE covers the columns 128 to 263, so 136 columns and 26 112 pixels in total. The LFE uses a linear pulse amplification in front of the discriminator, which compares the charge sensitive amplifier signal to a threshold voltage. The discriminator is used with a time over threshold (ToT) counter, to convert the time signals to a digital signal.

4.3 Phase 2 ACF

In order to communicate with the RD53A chip and its LFE the CMS Tracker Phase2 Acquisition & Control Framework (Ph2-ACF) [32] has been developed. The Ph2-ACF uses a hardware setup of a FPGA board, called FC7 board, which is connected to the RD53A chip through a Display Port cable and to a PC via an ethernet cable. It also provides a software framework used for sending and receiving information to and from the chip. It contains several functions, called scans, for injecting charges into the chip, sending triggers and collecting registered hits, which are used for calibrations and measurements on the chip. The framework itself and a description of the scan functions can be accessed from [32]. Examples of important scans will be described in the following paragraphs.

4.3.1 Charge injection

The injection of charges in the chip is controlled by two parameters VCAL_MED and VCAL_HIGH, which set the voltage injected into the injection capacitance ΔV_{cal} by

$$\Delta V_{cal} = \text{VCAL\_HIGH} - \text{VCAL\_MED}. \tag{4.2}$$

The injection voltage ΔV_{cal} is an internal charge measurement. The conversion from ΔV_{cal} to a physical charge varies from chip to chip and needs to be calibrated prior to measurement. For an estimate, the conversion $1\,\Delta V_{Cal} \approx (10 \pm 1)\,\mathrm{e}^-$ can usually be used. In this thesis, all measurements will be presented in term of ΔV_{cal}.

4.3.2 Threshold and trimming

The threshold of a pixel characterizes the minimum charge it is able to accurately measure. Each pixel follows a similar response pattern called the s-curve. The s-curve shows the proportion of detected hits for different injected charges (or voltages ΔV_{cal}). The s-curve can be fitted to a function

$$f(x) = \frac{1}{2}\left(g\left(\frac{x-\mu}{\sqrt{2\sigma^2}}\right) + 1\right), \tag{4.3}$$

where

$$g(x) = \frac{2}{\sqrt{\pi}} \int_0^x \exp(-t^2)\mathrm{d}t. \tag{4.4}$$

An example of a fitted s-curve plot is shown in Figure 4.3. From this fit the threshold is defined as the value where $f(x) = \frac{1}{2}$, which is given by the parameter mu. This value corresponds to the charge which has a 50 % probability of being detected.

As discussed in section 3.4.1 the threshold varies between the individual pixels. The distribution of thresholds among the pixels it typically Gaussian. To get a similar behaviour of the pixels, the width of this threshold distribution needs be as narrow

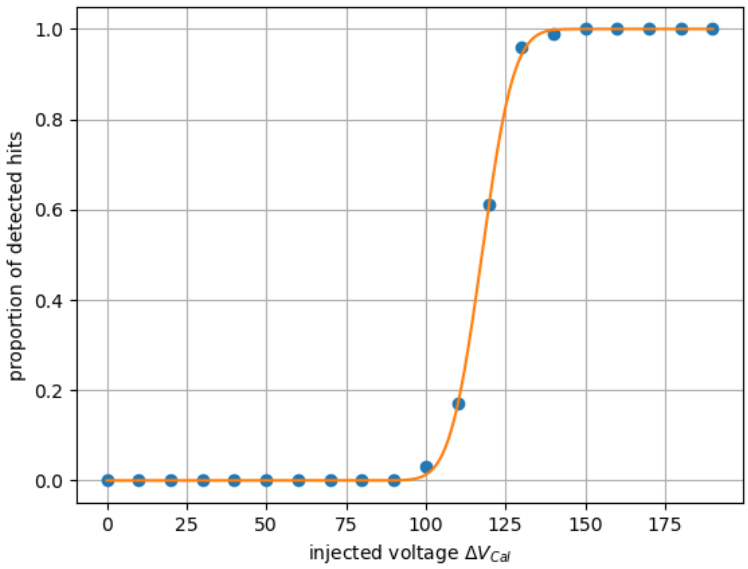

FIGURE 4.3: Typical s-curve plot. The blue dots indicate the proportion of measured hits (out of 100). The orange curve is a fit according to Equation 4.3.

as possible (typically the width of 40 electrons should be achieved [30]). Figure 4.4 shows an example of a threshold distribution. The s-curves and threshold distributions can be obtained in Ph2-ACF by performing a "scurve" scan. The position of the mean of the threshold distribution can be controlled by the integer parameter VTH_LIN. The width of the threshold distribution can be controlled by trimming the pixels. Each pixel can record a value between 0 and 15, stored as a 4-bit number, called TDAC. The chip can be trimmed by performing a "treshold equalization" scan which implements a binary search for the best TDAC value for each pixel.

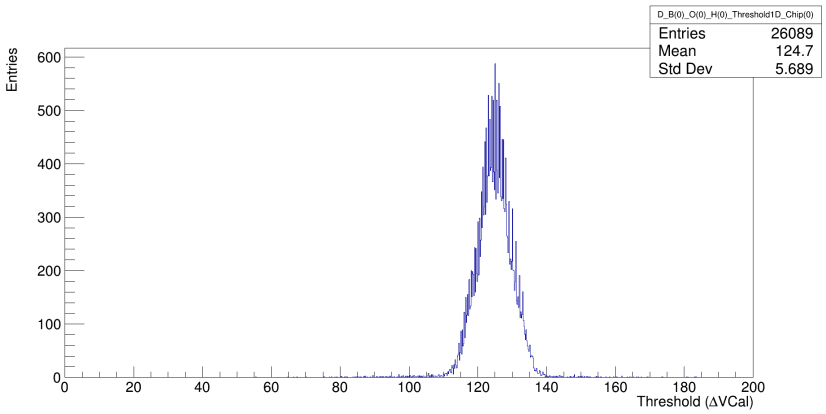

FIGURE 4.4: Threshold distribution of all pixels on the Linear Front End for a tuned detector. The x-axis shows the threshold value in ΔV_{cal}, the y-axis the number of pixels.

4.3.3 Gain

For an unknown charge generated by a particle traversing the sensor, the only information available is the signal strenght after the charge-sensitive amplifier. As explained in section 3.4.1, this signal is compared to a threshold signal by the discriminator and converted into time over threshold (ToT) information (see Figure 4.5).

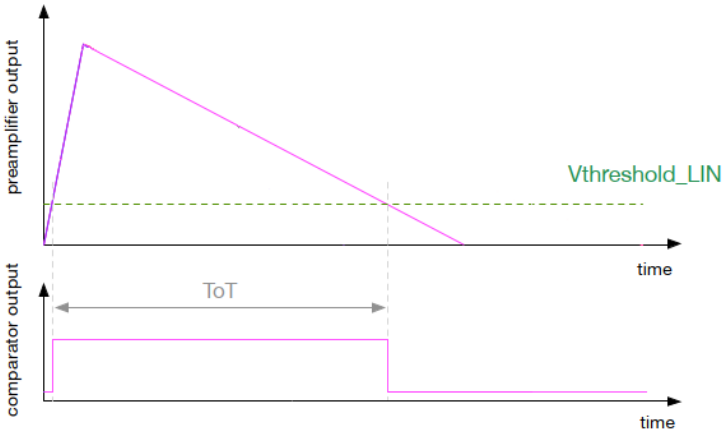

FIGURE 4.5: The signal from the preamplifier is compared to a threshold signal in the discriminator. The output signal of the discriminator is converted into time over threshold information. Figure reproduced from [33].

The ToT information is digitized and stored in four bits as values between 0 and 14 (not all bit values are used for storing ToT). To find the number of induced charges in a pixel a calibration of the ToT values is needed. This calibration can be performed by doing a "gain" scan in Ph2-ACF. This scan repeatedly injects charges over a large range into the pixels and records the mean ToT value for each injected charge value and each pixel individually. An example of a "gain" scan is shown in Figure 4.6. From the results of this scan a conversion between ToT values and charge in ΔV_{cal} can be computed. The details of this procedure will be discussed in section 4.3.4.

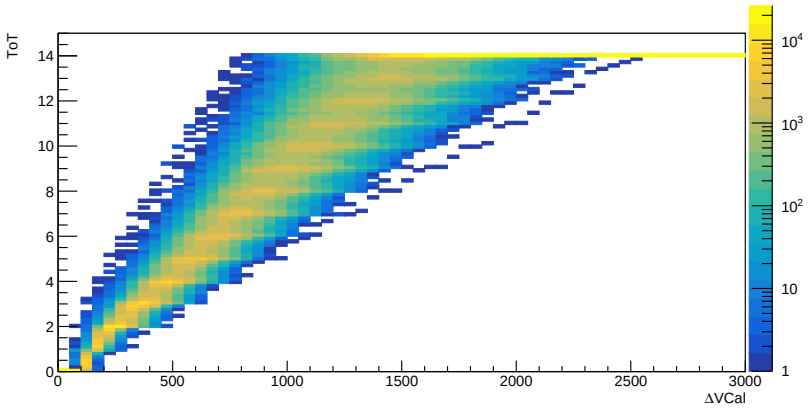

FIGURE 4.6: Result of an example "gain" scan. The histogram bins the measured mean ToT value for a given charge ΔV_{cal} for each pixel.

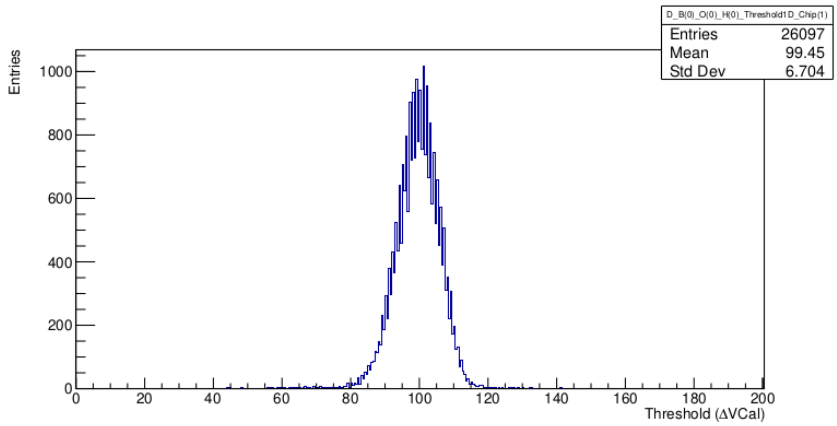

FIGURE 4.7: Threshold distribution for the chip trimmed to a low threshold used for the ToT calibration and measurments. The mean threshold is $\mu = 99\,\Delta V_{Cal}$, and the standard deviation $\sigma = 6.7\,\Delta V_{Cal}$.

4.3.4 Charge calibration

For the charge calibration, the chip was tuned to a low threshold and the same tuning will be used for any measurement. The threshold distribution is shown in Figure 4.7. The mean threshold is $\mu = 99\,\Delta V_{Cal}$, and the standard deviation $\sigma = 6.7\,\Delta V_{Cal}$.

The results of the gain scan for three example pixels is shown in Figure 4.8. The behaviour is not linear over the whole ToT range for a single pixel. For small ToT values, the slope is larger than for higher ToT values. For high ToT values the behaviour can be approximated as linear. The ΔV_{cal} range for a given ToT value is broad, justifying the need for per pixel calibration. The green points reach the maximum ToT value of 14 at $\approx 1000\,\Delta V_{Cal}$, while the light blue points reach it at $\approx 1500\,\Delta V_{Cal}$ and the dark blue ones at $\approx 2300\,\Delta V_{Cal}$.

The goal of the ToT calibration is to find a ΔV_{cal} value for each ToT value for each pixel. For ToT values between 0 and 13, the ΔV_{cal} value for ToT value i was calculated as the mean of all ΔV_{cal} values with ToT between i and $i+1$. This is equivalent to a linear fit for all points with ToT between i and $i+1$ and then using the ΔV_{cal} value from the fit corresponding to ToT value $i+0.5$. This method does not work for the maximum value ToT value of 14 since no ToT values larger than 14 can be measured. To get a ΔV_{cal} value for a ToT value of 14 a linear fit of the calculated points corresponding to ToT values between 11 and 13 is extrapolated to the ToT value 14. The calibration points for the three example pixels found with this method are represented as stars in Figure 4.8. The distribution of the calibration points for all pixels is shown in Figure 4.9.

During the analysis of the testbeam data, an issue with the gain scan was noticed, which is most likely caused by the readout chip. The pixel by pixel differences in the conversion from ToT to ΔV_{cal} are caused by slight performance differences (e.g. the amplification or noise level) of the charge sensitive amplifiers in each pixel. Over the whole pixel matrix, these differences should be randomly distributed, and thus also the charge value in ΔV_{cal} for a given ToT value should be randomly distributed and not depend on the position on the chip. Figure 4.10 shows the ratio of the mean charge value in every column and the mean charge value across the whole chip for each ToT value. For each ToT value, yellow areas indicate a larger reported charge

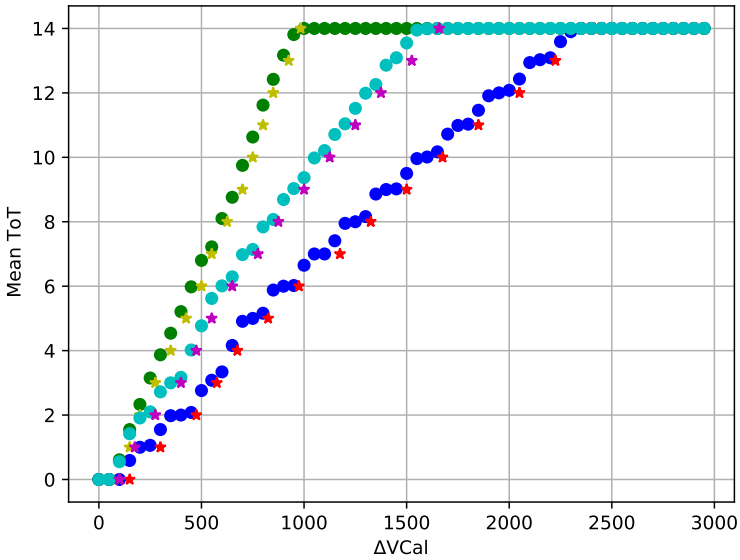

FIGURE 4.8: Results of gain scan for three example pixels. The stars represent the calculated calibration points used for the conversion from ToT to ΔV_{cal}. The examples show that the ToT calibration needs to be done per pixel, since the slopes are very different for the individual pixels.

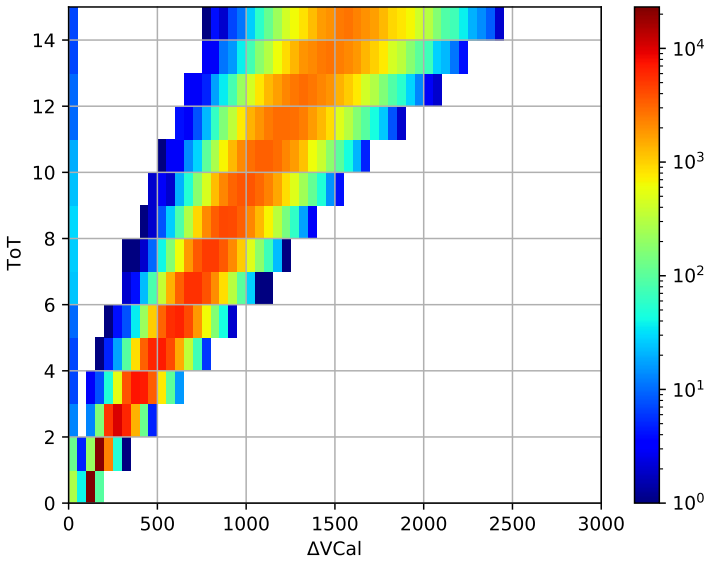

FIGURE 4.9: Distribution of ToT calibration points for all pixels on the linear front end.

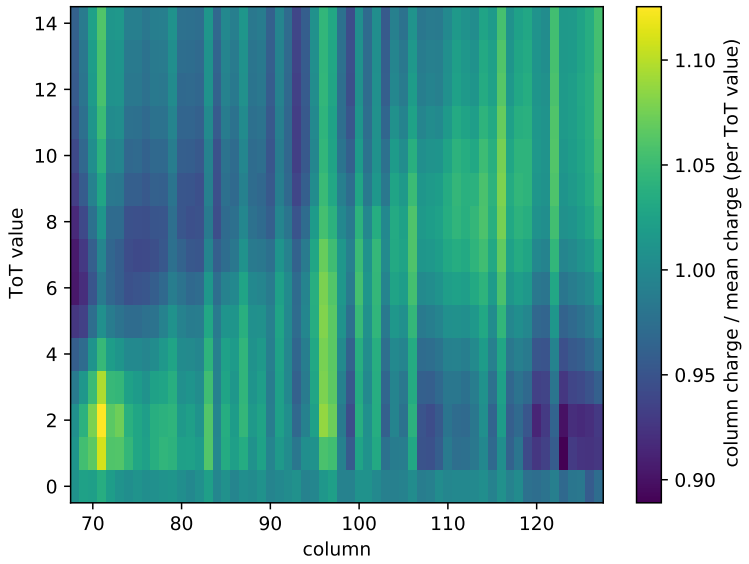

FIGURE 4.10: Ratio of mean charge per column and the mean charge across the whole pixel matrix for each ToT value. Areas of larger and smaller charge depending on the column number for a given ToT value can be seen. Thesse areas also move to larger column numbers with increasing ToT value, resulting in a wave-like pattern.

for the ToT value, dark areas indicate a smaller ToT value. A clear dependence of the charge on the column number can be seen, with variations of up to $\approx$ 10 %. The spatial dependence also seems to change with increasing ToT value. The areas with larger/smaller charge move to higher column numbers with increasing ToT value, resulting in a wave like pattern across the pixel matrix. This behaviour was seen on at least two modules with a RD53A readout chip but sensors from different manufacturers. Therefore this behaviour is most likely caused by the readout chip, e.g. by inconistent powering of the different columns. Further investigations are necessary on the cause of this problem and whether it persists in the successing RD53B/CROC readout chips.

4.4 Passive CMOS sensors

University of Bonn, ETH Zürich and University of Zürich have developed passive CMOS n-in-p pixel sensors in 150 nm technology, which are considered for the Phase-II Upgrade of the CMS pixel detector. The sensors are produced using lithography stitching, which allows for a more flexible production and larger sensor sizes than normal lithography production. Without stitching, the maximum sensor size is constrained by the maximum reticle size and the field of view of the lithographic equipment. In stitching processes, multiple reticles with individual function blocks are used instead of one reticle for the whole sensor. The sensor is then gradually built by building the function blocks step by step, realigning the wafer and reticle after each function block. A schematic of such a reticle containing functions blocks for a center piece, top and bottom edges, left and right edges, corner edges and small test structures is shown in Figure 4.11. Figure 4.12 shows how a sensor is built from the individual function blocks. The edges where two function blocks come together

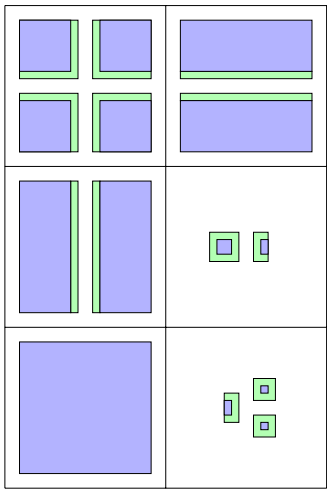

FIGURE 4.11: Schematic of a reticle used for stitching. The reticle contains function blocks for corners (top left), top and bottom edges (top right), left and right edges (middle left), center pieces (bottom left), and test structures (middle and bottom right).

are called stitching lines. The function blocks are designed with an overlap of the order of a few 100 nm which ensures that the correct structures are built and no gaps are created. A microscope image of the edge of one of the passive CMOS sensors with a pixel size of 100 µm $\times$ 25 µm is shown in Figure 4.13 (the first two rows have 50 µm $\times$ 50 µm pixels as the function blocks for the edges of a 50 µm $\times$ 50 µm pixel sensor were reused). Two stitching lines can be seen as darker lines. One vertically in the middle, one horizontally between the second and third row of pixels. All stitching lines go between two pixels through the p-stop. The stitching line is visible in the areas where no structures are placed, as these areas are covered with so called metal fill (small metal rectangles) for production purposes only. Close to the stitching line, no metal fills are placed, which makes the stitching lines visible. In areas with structures, the stitching line is invisible due to the 200 nm overlap of the function blocks.

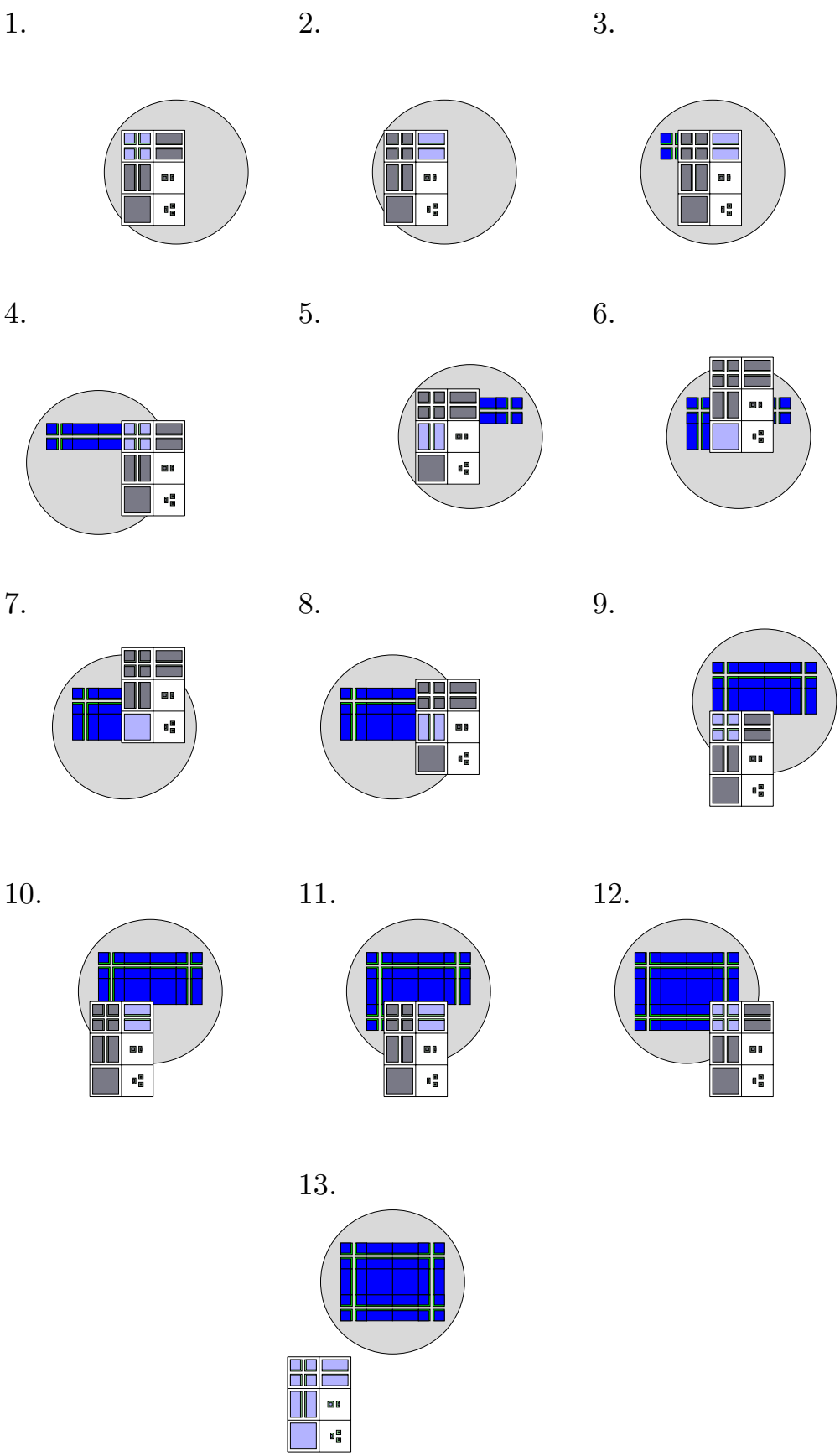

FIGURE 4.12: Schematic of the production of a full sensor from individual function blocks in a stitching process.

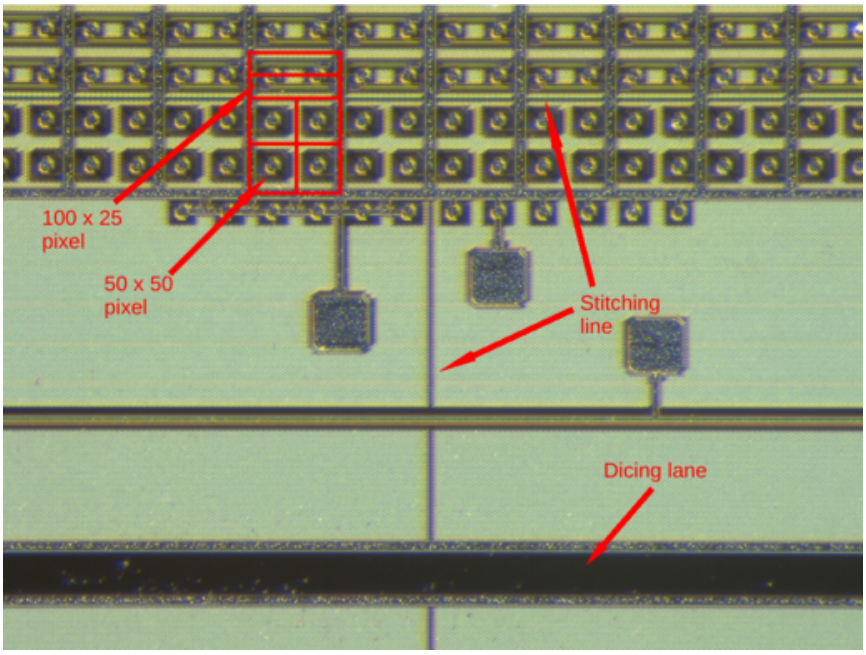

FIGURE 4.13: Microscope image of the edge of a passive CMOS sensor. Two stitching lines are visible (vertically in the middle and horizontally between the second and third row of pixels. The stitching lines is visible since no metal fills are placed there in region where no structures were built. In regions with structures the stitching line is invisible.

Chapter 5

Data acquisition

5.1 Testbeam setup

A testbeam is a beam of minimum ionizing particles from an accelerator which is used to illuminate a device under test (DUT). Testbeams are used to simulate the working environment of a detector and test it in a realistic scenario. For pixel detectors a beam telescope is used to measure quantities such as the detection efficiency or the spatial resolution of the device. A beam telescope itself consists of several plains of high granularity tracking detectors. By reconstructing the primary tracks of the testbeam on the telescope planes, one can infer the position of the track on the DUT.

For the data acquisition, a high resolution EUDET/AIDA pixel beam telescope [34] with five Mimosa26 pixel detectors and one FE-I4 acting as time reference plane have been used at the H6 beamline at SPS at CERN. The H6 beamline provides a beam of pions with an energy of 120 GeV. The DUT was placed in a box of 6 cm thick polystyrene for cooling and could be turned around the vertical axis to simulate different angles of incidence. A picture of the telescope setup is shown in Figure 5.1 and a sketch indicating the z-positions (along the beam) of each plane is shown in Figure 5.2.

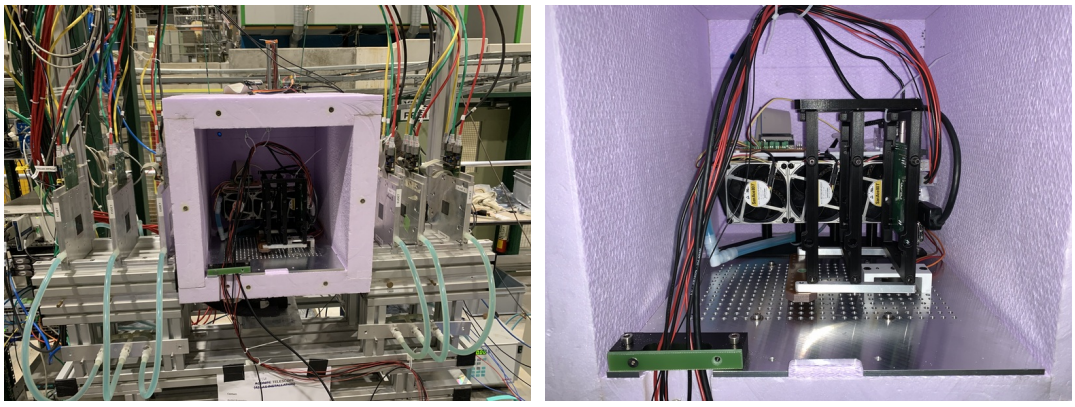

(A) Full view of the telescope setup. The DUT is inside the pink cooling box in the middle. The telescope planes are positioned to the left and right of the box.

(B) DUT inside the cooling box. The DUT can be placed in two different orientations and can be turned around the vertical axis to simulate different incidence angles.

FIGURE 5.1: Beam telescope setup at the H6 beamline at CERN. The beam is incident from the left in both picture.

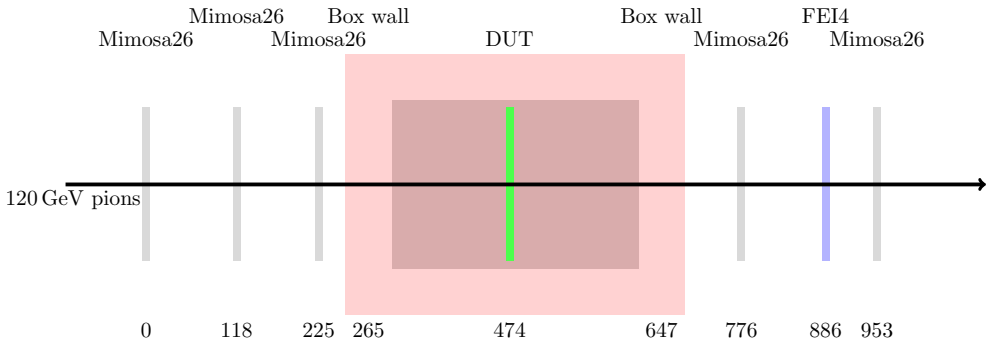

FIGURE 5.2: The z-positions of telescope planes, the DUT and the wall of the cooling box. All values are given in mm.

The Mimosa26 detector is a monolithic active pixel sensor (MAPS) and consists of 576×1152 pixels of size $18.4\,\mu m \times 18.4\,\mu m$ covering a total active area of $224\,mm^2$. The Mimosa26 has an integration time of $115.2\,\mu s$, which is several orders of magnitude longer than the 25 ns integration time of the RD53A chip. This would lead to ambigous matching of telescope tracks to hits in the DUT. For this reason a ATLAS hybrid pixel assembly based on the FE-I4 chip is used as a timing plane. The FE-I4 chip also has an integration time of 25 ns and consists of 80×336 pixels of size $250\,\mu m \times 50\,\mu m$. A hit on the FE-I4 plane serves as a trigger, which is sent to a custom Trigger Logic Unit (TLU). The TLU then sends the trigger to the Mimosa26 telescope planes and the DUT and requests data collection. The data of all planes was acquired by the Data Acquisition software EUDAQ [35]. The central part of EUDAQ is the Data Collector, which receives the data from the Producers which communicate with the different pieces of hardware and generate the data (e.g. Phase2-ACF for the RD53A chip). The Data Collector then merges the data from all detectors and writes it to a single file.

The data was taken during a testbeam from the 27^{th} October, 2021 to the 10^{th} November, 2021. An unirradiated passive CMOS sensor (12D6S13) flipchipped to the RD53A readout chip was used as DUT. The sensor has a pixel size of $100\,\mu m \times 25\,\mu m$ and a thickness of $150\,\mu m$. It was biased with a bias voltage of $-60\,V$ for full depletion and data was taken at incience angles between 0° and 12° along the short pixel pitch. For the analysis of the stitching region, 7.5×10^6 events have been analysed for two angles (0 degree and 12°). For the analysis of the η-correction, 10^6 events have been analysed for each angle between 0° and 12°.

5.2 Track reconstruction and track selection

The data was reconstructed using the Corryvreckan track reconstruction and analysis software [36]. For the reconstruction of the test beam data, all of the detector planes have to be aligned in the software. Then the tracks can be reconstructed from the telescope planes and hits on the DUT can be associated with individual tracks. This is done in several steps, which will be described below.

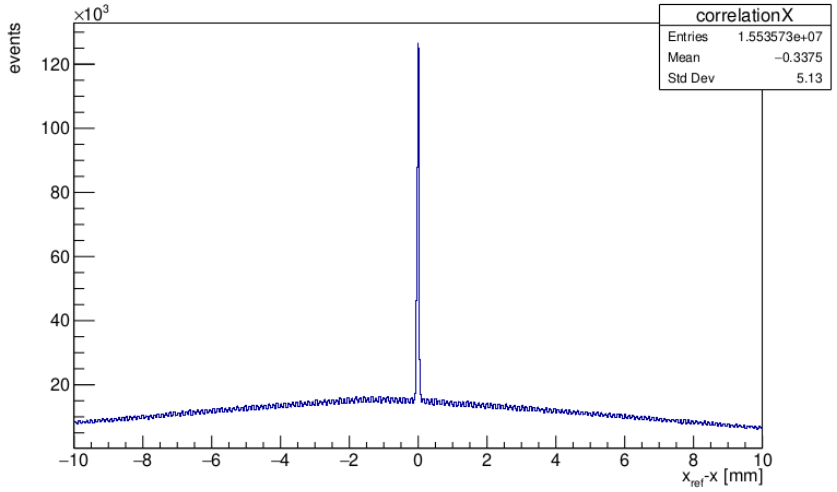

FIGURE 5.3: Example of a 1D correlation histogram. The position of the maximum value defines the translational shift of the plane in the prealignment step.

5.2.1 Prealignment

First, all planes are roughly translationally aligned along the X and Y axes with respect to a reference telescope plane, which was chosen to be the first plane facing the beam. The prealignment uses correlations, which are the differences in global X- and Y-direction between the detected hits on each plane and the refernce plane. The maximum of the 1D correlation histogram is used to determine the translational shift in the X- and Y-direction with respect to the reference plane. Figure 5.3 shows an example plot of a 1D correlation histogram.

5.2.2 Telescope alignment

Next, the five Mimosa26 telescope planes were aligned using a subset of 50 000 tracks. The tracks are modeled as straight lines with a detected hit cluster on each of the five planes. The cluster associated to a track on each plane has to be within a set spatial distance from the impact point of the track on the plane.

After the track reconstruction the telescope planes are translationally and rotationally aligned along the axis perpendicular to the beam direction by minimizing the χ^2 of all tracks. The minimization of the χ^2 is repeated three times, each time with refitted tracks according to the new detector positions. The whole alignment procedure is repeated twice with different spatial cuts for the track building. First with a spatial cut of 300 µm and then 50 µm in the second iteration.

After the alignment the residual distribution of the telescope planes can be checked. Figure 5.4 shows a comparison of the residual distribution on a telescope plane before and after the alignment. Both distributions are fit to a Gaussian model. After the alignment the residual distribution is well-centered and the width (the resolution on that plane) is improved by approximately 10 %.

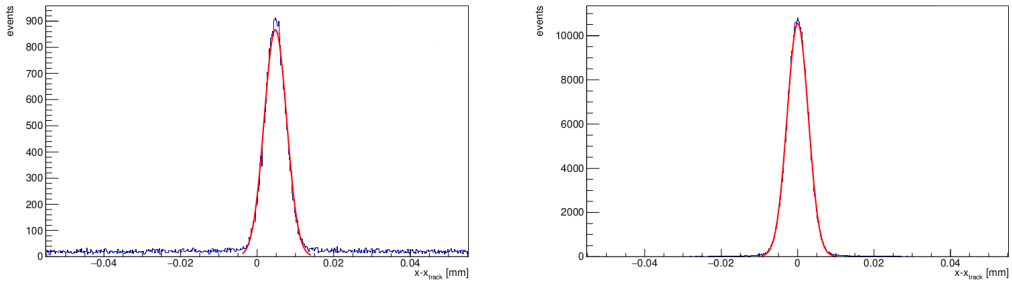

(A) Before the alignment.

(B) After the alignment.

FIGURE 5.4: Histograms of the residuals on a telescope plane before and after the alignment. After the alignment, the residuals are well-centered and the width is reduced.

5.2.3 DUT and FE-I4 alignment

The DUT and time reference plane (FE-I4) are aligned independently in a next step using a subset of 20 000 events. The track building is again solely done on the five telescope planes with a spatial cut of 50 µm. This results in approximately 300 000 tracks which are available for the alignment. After the track building on the telescope planes, clusters on the DUT and FE-I4 are matched to the tracks using a relative spatial cut for the cluster association. The relative cuts define an ellipse with multiples of the pixel pitch in X and Y as the semiaxes around the track. If the cluster center is within this ellipse, the cluster will be associated to the track.

Afterwards the DUT and FE-I4 are aligned by minimising the track χ^2 to obtain the translational and rotational shifts. The minimisation is repeated three times, each time with the newly calculated χ^2. This alignment procedure is again repeated twice, each time with different relative spatial cuts. The first time a relative cut of 10 pixel pitches is applied, the second time a relative cut of 6 pixel pitches is used.

5.2.4 Track selection and analysis

For the reconstruction of the data after the alignment, tighter cuts were applied to the clusters and tracks in order to minimise the influence of noise hits and close tracks on the FE-I4 time reference plane. Only clusters within three bunch crossings of the latency of the FE-I4 were accepted as particle hits on the FE-I4. Figure 5.5 shows a histogram of the bunch crossings on the FE-I4. Only clusters with a bunch crossing value between 0 and 2 were accepted in this case. Hits with a bunch crossing value larger than 2 are most likely due to noise hits in the FE-I4 or due to multiple tracks. These noise hits are not due to a particle passing through the detector and would contribute to fake tracks in the reconstruction, which will influence the efficiency measurement of the DUT.

The track reconstruction was again made on the five Mimosa26 planes with a tighter spatial cut of 25 µm. Additionally the tracks were required to be isolated on the time reference plane. To check the isolation a circle with 600 µm radius was placed around a track on the FE-I4. If a second track in the same event was found within this circle, both tracks were rejected.

For the association of hits on the time reference plane to the telescope tracks a tight spatial cut of 135 µm along the x-axis and 35 µm along the y-axis was applied to get

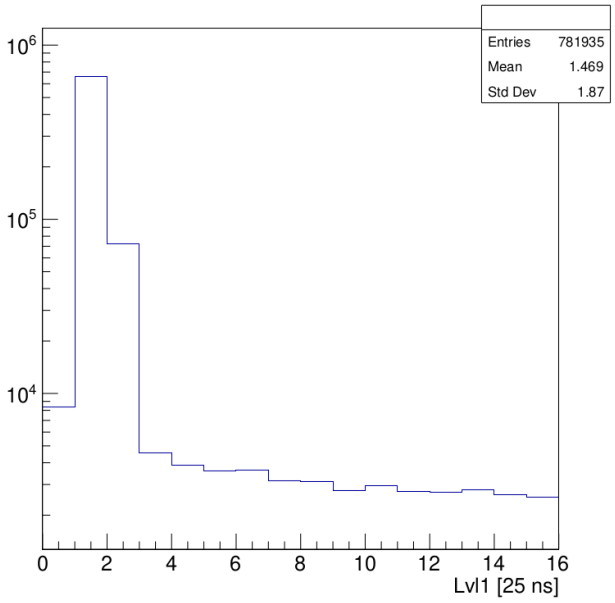

FIGURE 5.5: Histogram of bunch crossing number on the FE-I4 time refernce plane. For the reconstruction of the tracks, only hits within three bunch crossing of the latency were selected (here between 0 and 2).

only very clean tracks on the FE-I4. For the association of hits on the DUT a cut of 150 µm was applied in both directions.

Finally only tracks with an associated cluster on the time reference plane were analysed using the "AnalysisDUT" module. The requirement of an associated cluster on the time reference plane ensures that the reconstructed track occured at the same time as the readout of the DUT. Without the time reference plane, this would not be ensured due to the long integration time (115.2 µs) of the Mimosa26 planes. The global and local track positions on the DUT, hit information, global and local cluster positions, cluster sizes, cluster charges, pixel positions and pixel charges are saved for each analysed track for the further analyses presented in chapter 6 and chapter 7.

Chapter 6

Impact of stitching on sensor performance

The impact of stitching was investigated using testbeam data with a 120 GeV pion beam of an unirradiated passive CMOS sensor connected to a RD53A readout chip. The sensor had a pixel size of 100 µm × 25 µm and a thickness of 150 µm and was biased with −60 V to full depletion. The effects of stitching are expected to be largest in unirradiated sensors due to the lower bias voltage and thus lower electric fields inside the sensor than compared to irradited sensors.

One stitching line of the passive CMOS sensors is located between the columns 99 and 100. To investigate the impact of the stitching process on the performance of the detectors, the mean cluster size, charge collection, charge diffusion and detection efficiency of these two columns were compared to columns of pixels without a stitching line between them. The analysis was made for runs with orthogonal (0°) beam incidence and 12° beam incidence along the short pixel pitch. In total 7.5×10^6 each events were analysed for both angles.

Due to the spatial dependences of the ToT calibration, which were discussed in section 4.3.4, only the columns 101 to 104 were used for the comparison. These columns are close to the columns 99 and 100 and therefore the effect of the spatial dependence of the ToT calibration can be neglected. The neighbouring columns smaller than 99 were not used, since the columns 96 and 97 generally show a larger charge (see Figure 4.10).

In total, the dataset for the stitched pixels contains approximately 40 000 tracks, the dataset for the non-stitched pixels contains approximately 80 000 tracks.

The quantites are shown in in-pixel histogram plots. These plots show the given quantity dependent on the impact position of the reconstructed track within the pixel. All plots show two pixels next to each other. For the stitched pixels (columns 99 and 100) the stitching line is located at $x = 0$. For the stitched and non-stitched pixels, the left half of the histogram corresponds to odd column numbers (99, 101 and 103) the right half corresponds to even column numbers (100, 102 and 104).

6.1 Cluster size

The 2D histogram maps of the mean cluster size for orthogonal incidence are shown in Figure 6.1. A 1D histogram along the x-axis is shown in Figure 6.2. The errorbars in this histogram show the standard deviation of the mean cluster size. The cluster

size distributions in Figure 6.1 also show the expected shape for a beam with orthogonal incidence. In the center of the pixels, mostly clusters of size one are detected, since the particle traverses only the single pixel and the spread of the charge cloud is not large enough for charge sharing with other pixels. Closer to the edges mostly two-pixel clusters are detected as charge sharing between neigbouring pixels is effective close to the edge. In the corners, also clusters with sizes three and larger are detected more often due to charge sharing with three and more pixels.

From both the 1D and 2D histograms, no difference can be seen between the stitched pixels and the non-stitched pixels. Especially for the bins close to the edge of the single pixels towards the stitching line at $x = 0$ no difference between the two sets can be observed.

Also for the measurements with an angle of 12°, shown in Figure 6.3 and Figure 6.4, no difference can be observed for the cluster size between the stitched and non-stitched columns. The distributions in Figure 6.3 follow the expected pattern for an incidence of 12°. In every position the mean cluster size is measured to be at least two as is predicted by the geometry of the pixels (for angles larger than $\arctan(\frac{25\,\mu m}{150\,\mu m}) \approx 9.5°$ the particle will always pass through at least two pixels, see also Figure 6.5). Close to the short edges ($x = 0$ and $x = \pm 100\,\mu m$) charge sharing increases the cluster size to three, similarly as for the orthogonal measurements. For track positions $y = 0$ and $y = -5\,\mu m$ a small increase in the cluster size is detected. This can be explained by the alignment. The alignment procedure described in section 5.2 uses the charge weighted mean position of the clusters for the alignment. Assuming a constant rate of ionization, this corresponds to the position the particle passes the middle of the sensor. As can be seen from Figure 6.5, a track passing through the middle at $y = 0$ will pass through three pixels, which increases the mean cluster size. A track passing at a slightly smaller y-position (more to the right in the Figure 6.5) deposits more charge close to the n-implant of the right pixel and only a small charge in the left pixel. Due to diffusion in the unirradiated sensor, part of the charge is able to move from the pixel in the middle into the pixel on the left, while drifting towards the implants. This diffusion charge is in some cases able to create a signal in the pixel on the left, increasing the cluster size. For a track with a slightly larger y-position (more to the left), only a small charge is created in the right pixel and the path to the implants is not long enough for a signal from diffused charges. Thus only the pixel in the middle and on the left will collect a charge and see a hit and the cluster size will stay only at 2. This will also result in an offset in the residual distribution as the charge created in the right pixel is lost.

6.2 Charge collection

The results for the collected charge for an incidence angle of 0° are shown in Figure 6.6 and Figure 6.7. The charge distribution in each bin was fitted with a convolution of a Landau distribution and Gaussian kernel and the most probable value (mpv) of the Landau contribution was determined and is shown. The data does not follow a pure Landau distribution (see section 3.1), since detector resolution and noise effects from the readout electronics give rise to a Gaussian broadening of the charge distribution, which is accounted for by the Gaussian Kernel in the fit. An example of a charge distribution for the bin located at $x = -37.5\,\mu m$ in Figure 6.7 is shown in Figure 6.8. The errors bars shown in Figure 6.7 are the uncertainties of the mpv obtained from the fit to the distribution. The expected mpv charge produced

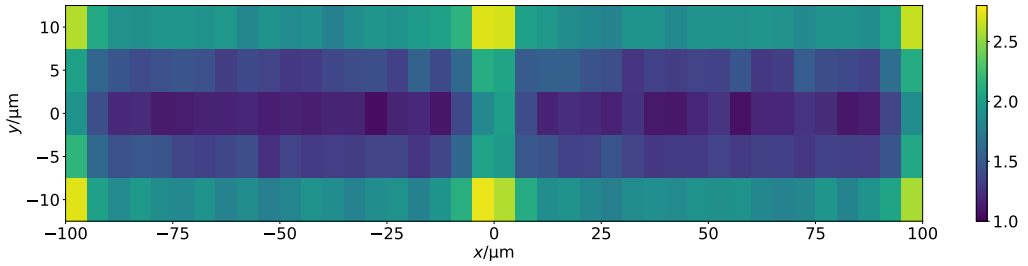

(A) Stitched

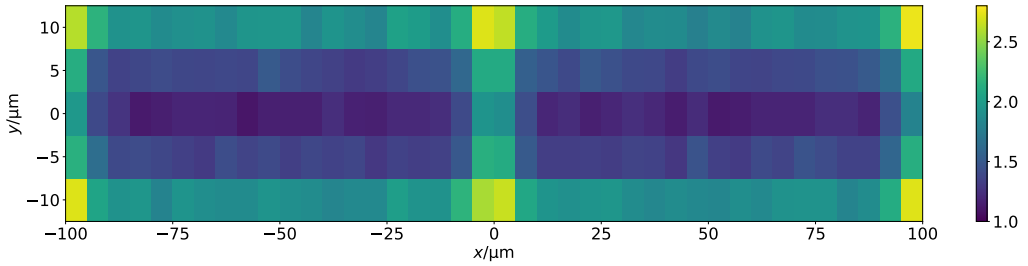

(B) Non-stitched

FIGURE 6.1: Mean cluster size 2D histograms for 0° incidence for stitched (A) and non-stitched (B) pixels. The distribution follows the expected shape. No difference can be observed between the stitched and non-stitched pixels.

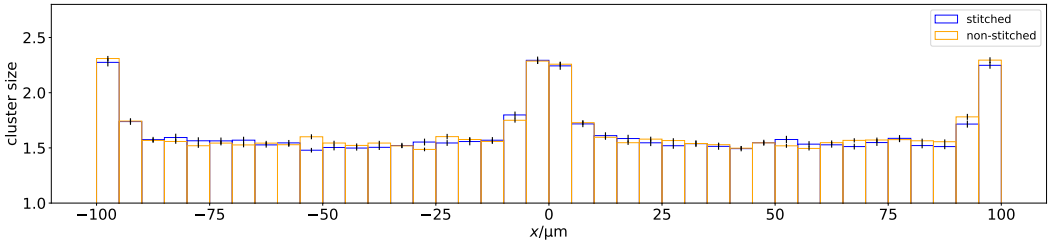

FIGURE 6.2: Mean cluster size histogram for 0° incidence for stitched and non-stitched pixels. The error bars represent the standard deviation of the mean cluster size in each bin. No difference can be observed between the stitched and non-stitched pixels.

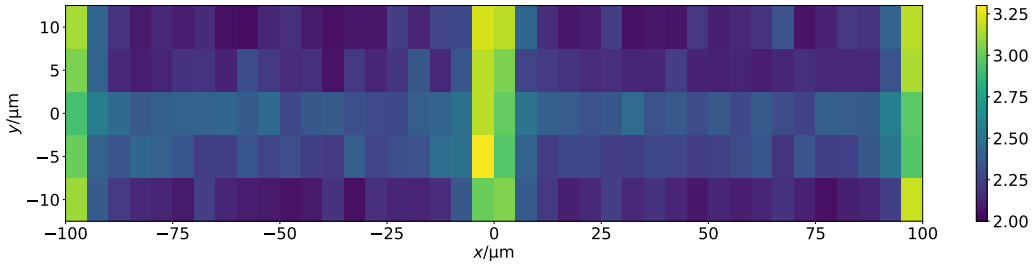

(A) Stitched

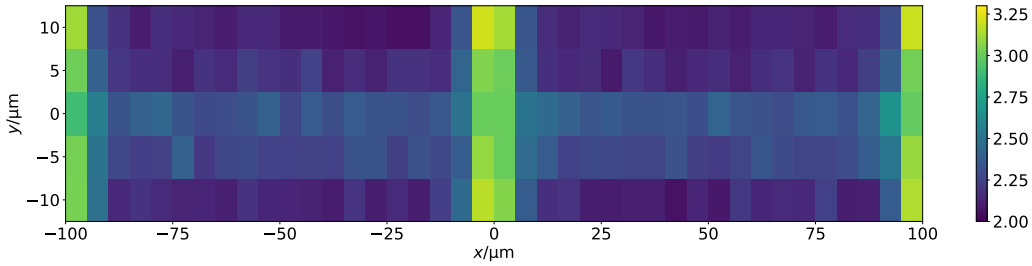

(B) Non-stitched

FIGURE 6.3: Mean cluster size 2D histograms for 12° incidence for stitched (A) and non-stitched (B) pixels. The distribution follows the expected shape. No difference can be observed between the stitched and non-stitched pixels.

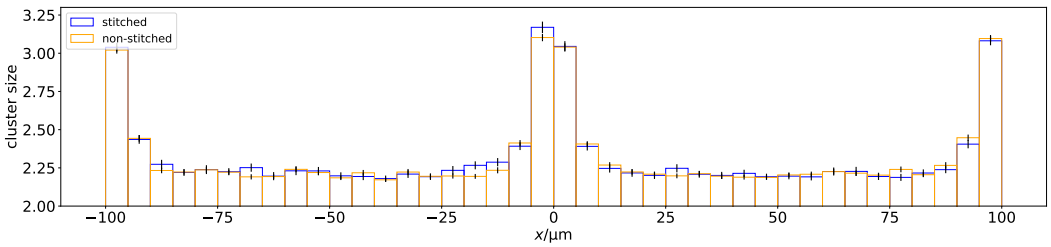

FIGURE 6.4: Mean cluster size histogram for 12° incidence for stitched and non-stitched pixels. The error bars represent the standard deviation of the mean cluster size in each bin. No difference can be observed between the stitched and non-stitched pixels.

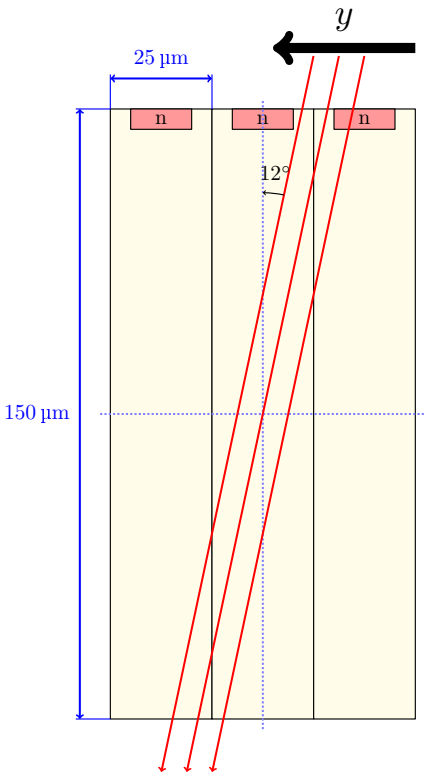

FIGURE 6.5: Cross section of the sensor. The particles (red lines) pass through the sensor from above. The created charges are collected at the n-implants at the top. The indicated y-direction corresponds to the y-direction in Figure 6.3.

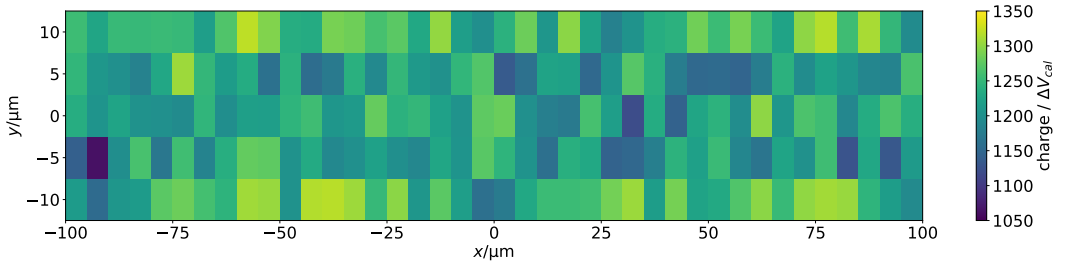

(A) Stitched

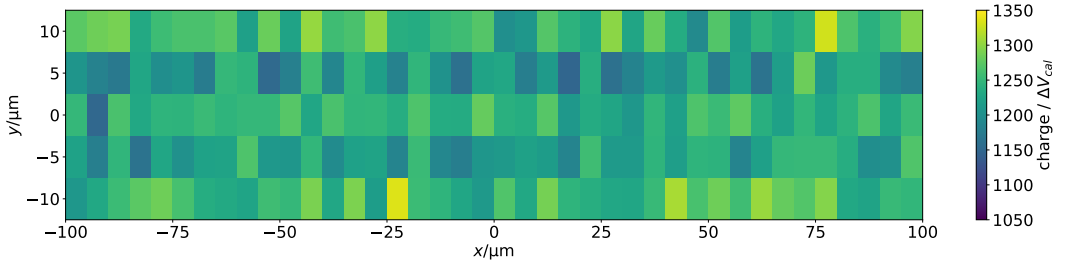

(B) Non-stitched

FIGURE 6.6: Most probable value of the collected charge for 0° incidence for stitched (A) and non-stitched (B) pixels. No difference can be observed between the stitched and non-stitched pixels.

by minimum ionizing particles in silicon is $75\,e^-/\mu m$ (see section 3.1). For a sensor with thickness 150 µm, this corresponds to a charge of $11\,250\,e^-$. The measured collected charge of $1250\,\Delta V_{Cal}$ in Figure 6.6 and Figure 6.7 is in within the range of the expected signal, depending on the charge calibration of the individual readout chip. No difference between the stitched and non-stitched pixels can be seen from the 1D and 2D histograms.

The results for the 12° incidence are shown in Figure 6.9 and Figure 6.10. The data was obtained in the same way, by fitting a convolution of a Landau distribution with a Gaussian kernel to the charge distribution in each bin and extracting the mpv of the Landau. The expected charge for 12° incidence is $11\,500\,e^-$ which is a bit larger due to the longer path of the particles. The observed mpv charge is approximately $1300\,\Delta V_{Cal}$, which is about $25\,\Delta V_{Cal}$ above the expectation. The reason for this is probalbly that mostly two hit clusters are recorded for this angle. As the ToT values have a maximum of 14, the largest possible charge per pixel is limited. For two pixel clusters large charges have a higher chance of being fully measured, which might populate the tail of the charge distribution more and shift the MPV upwards. Nonetheless, to check this, a charge calibration of the module would be needed to convert the charges from ΔV_{cal} to electrons and compare them to the expected signal. From both Figure 6.9 and Figure 6.10 no difference between the stitched and non-stitched pixels can be seen.

6.3 Charge diffusion

As the stitching line is located between two adjacent pixel columns it is interesting to compare the charge diffusion across the stitching line to the diffusion in the non-stitched regions. This gives a direct test of any effects of the stitching on the charge

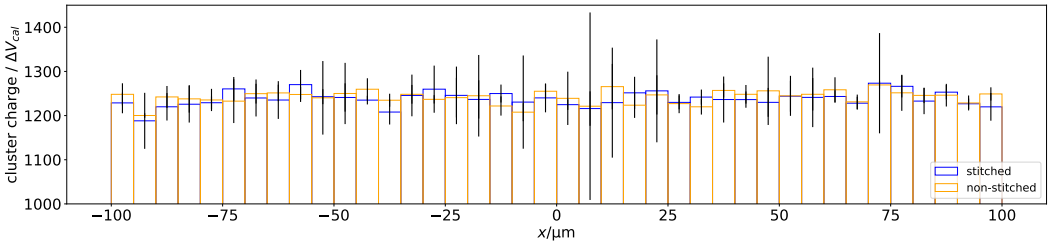

FIGURE 6.7: Most probable value of the collected charge for 0° incidence for stitched and non-stitched pixels. The error bars represent the uncertainty on the mpv charge from the fit. No difference between the stitched and non-stitched pixels can be observed with in the statistical limits.

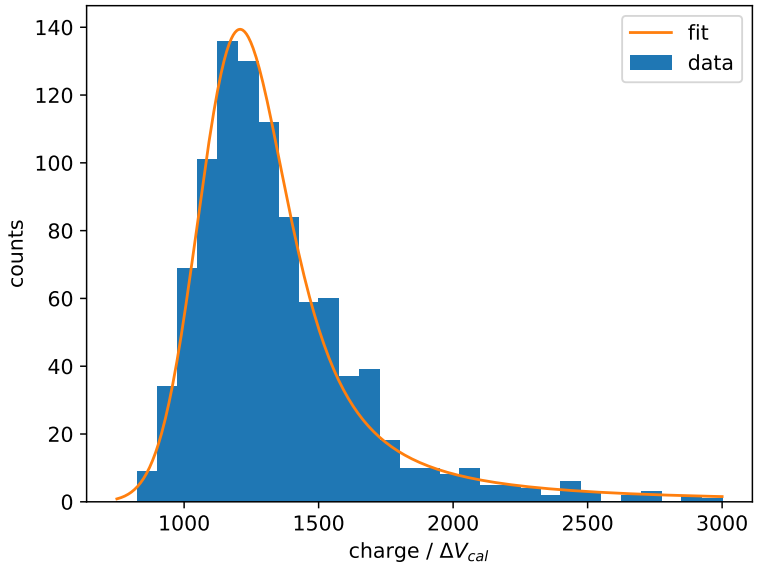

FIGURE 6.8: Charge distribution histogram for the bin located at $x = -37.5\,\mu m$ in Figure 6.7 for orthogonal incidence. The distribution was fit with a convolution of a Landau distribution and a Gaussian kernel.

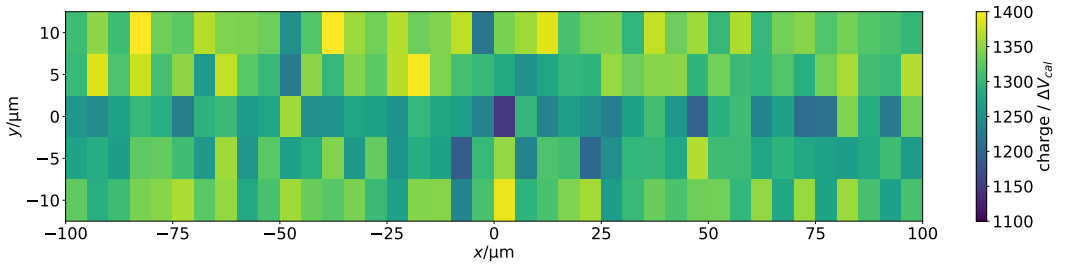

(A) Stitched

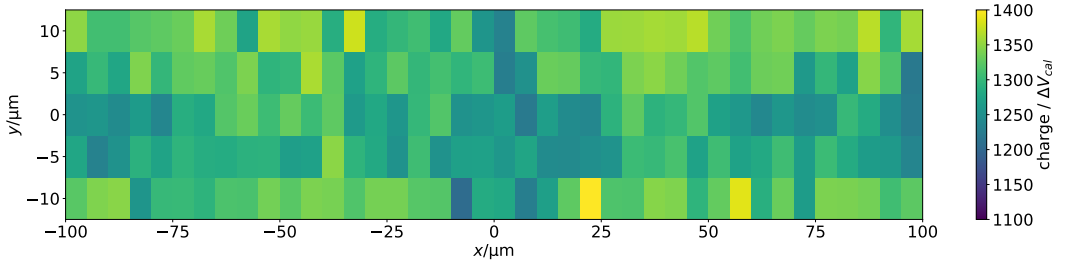

(B) Non-stitched

FIGURE 6.9: Most probable value of the collected charge for 12° incidence for stitched (A) and non-stitched (B) pixels. No difference can be observed between the stitched and non-stitched pixels.

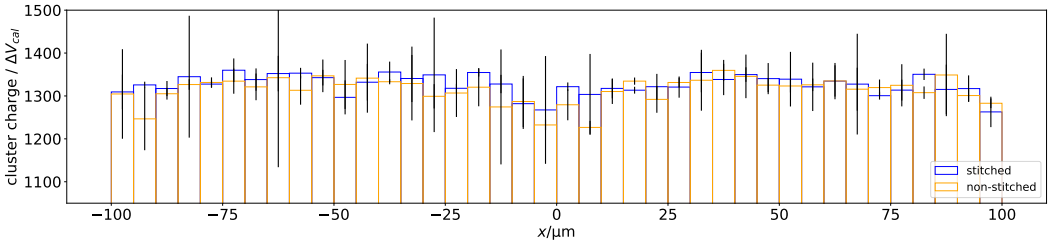

FIGURE 6.10: Mean charge collection 2D histograms for 12° incidence for stitched and non-stitched pixels. The error bars represent the uncertainty on the mpv charge from the fit. No difference between the stitched and non-stitched pixels can be observed with in the statistical limits.

collection of the pixels. The results for the measurement of the diffusion of charges across the stitching line are shown in Figure 6.11 for orthogonal incidence. For these histograms, only clusters of size two with a track position with $|x| < 10\,\mu m$ were selected. The seed pixel is defined as the pixel which was hit by the reconstructed track. Figure 6.11a shows the charge distribution in the seed pixels, Figure 6.11b shows the charge distribution in the second pixel across the edge. The error bars present the Poissonian statistical errors in each bin. Again, no difference within the statistical errors between the stitched and non-stitched pixels can be observed.

6.4 Efficiency

The detection efficiency of the pixels can be measured using the reconstructed tracks from the telescope. The efficiency is simply given by the number of tracks with an associated cluster on the DUT divided by the total number of tracks on the DUT. The 2D and 1D histograms for the detection efficiency measurement are shown in Figure 6.12 and Figure 6.13 for 0° incidence and Figure 6.14 and Figure 6.15 for 12° incidence. The error bars in the 1D histograms show the Clopper-Pearson confidence intervals [37] for the efficiency in each bin. No difference between stitched and non-stitched pixels can be observed within the statistical limits. The 2D histograms show more bins with an efficiency of 1 for the stitched pixels than for the non-sitched ones. This is purely due to the difference in the number of available tracks for each type. Twice as many tracks were analysed for the non-stitched pixels than for the stitched pixels, which results in twice as many bins that loose a single track when assuming equal efficiency.

Both stitched and non-stitched pixels reach for all bins an efficiency well above the requirement of 99 % set for the Phase-II Upgrade of the pixel detector (see section 2.2.3 or Table 4.1).

6.5 Summary

The impact of stitching on sensor perfomance of unirradiated passive CMOS sensors was tested for important sensor parameters. Two pixel columns adjacent to the stitching line were compared to four columns without stitching for two incident angles of 0° and 12°. The 1D and 2D distributions of cluster size (section 6.1), collected charge (section 6.2), charge diffusion (section 6.3) and efficiency (section 6.4) follow the expected behaviour for both stitched and non-stitched pixels and for both incident angles. No difference between the stitched and non-stitched pixels could be measured for the tested quantites. Additionally, the efficiency requirement of 99 % for the Phase-II Upgrade of the CMS pixel detector is met by both the stitched and non-stitched pixels.

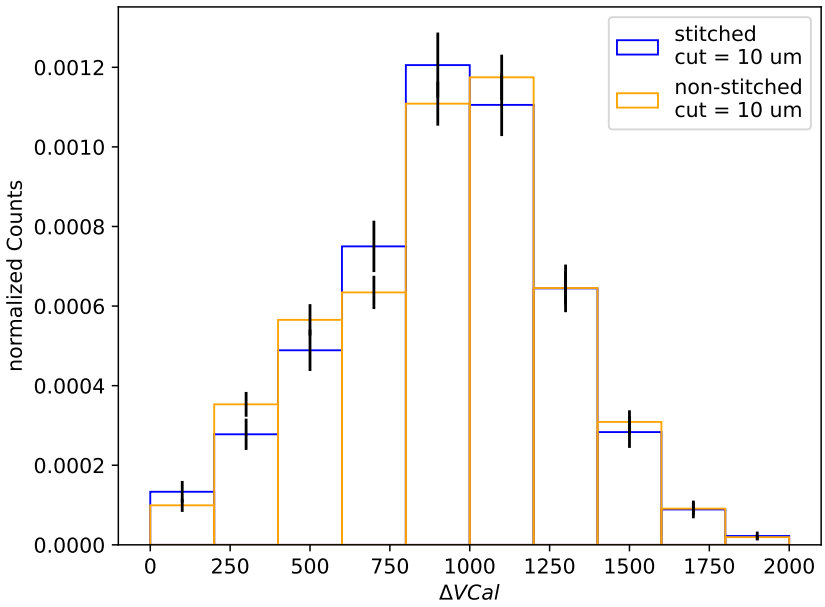

(A) Seed charge

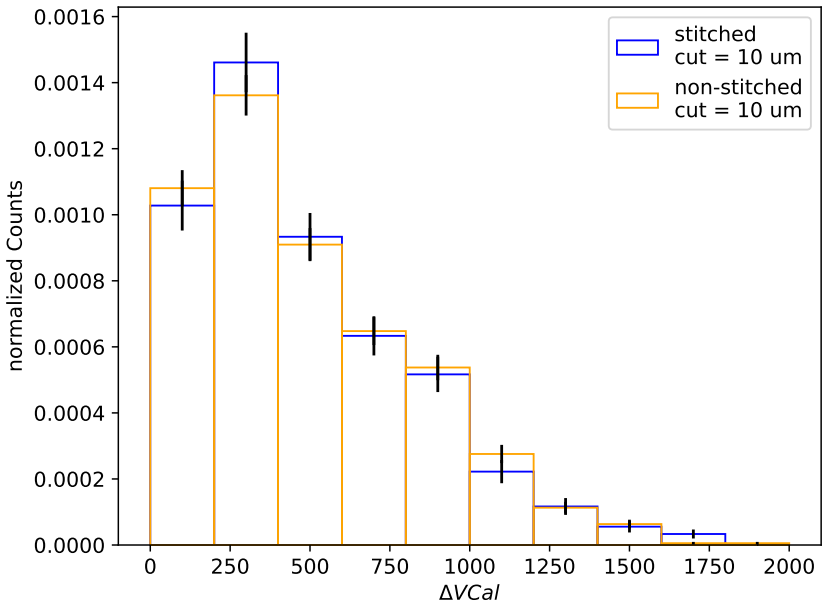

(B) Diffused charge

FIGURE 6.11: Charge distributions in seed pixel and secondary pixel for two hit clusters with track position $|x| < 10\,\mu m$ and orthogonal incidence. The error bars represent the statistical Poissonian errors of each bin. No difference between the stitched and non-stitched pixels can be observed within the statistical uncertainties.

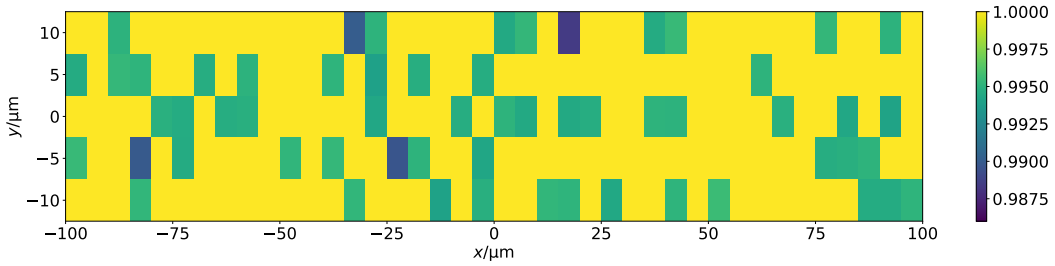

(A) Stitched

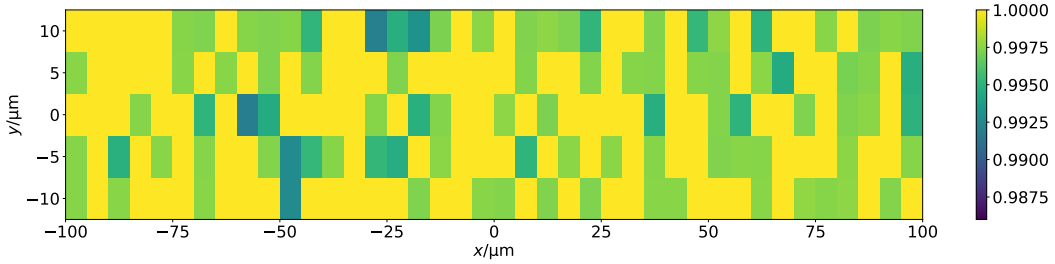

(B) Non-stitched

FIGURE 6.12: Measured efficiencies for 0° incidence for stitched (A) and non-stitched (B) pixels. No difference can be observed between the stitched and non-stitched pixels.

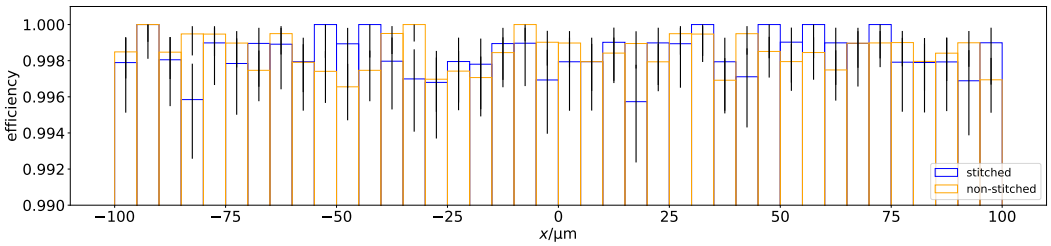

FIGURE 6.13: Measured efficiencies for 0° incidence for stitched and non-stitched pixels. The error bars represent the Clopper-Pearson confidence intervals for the efficiencies. No difference between the stitched and non-stitched pixels can be observed with in the statistical limits.

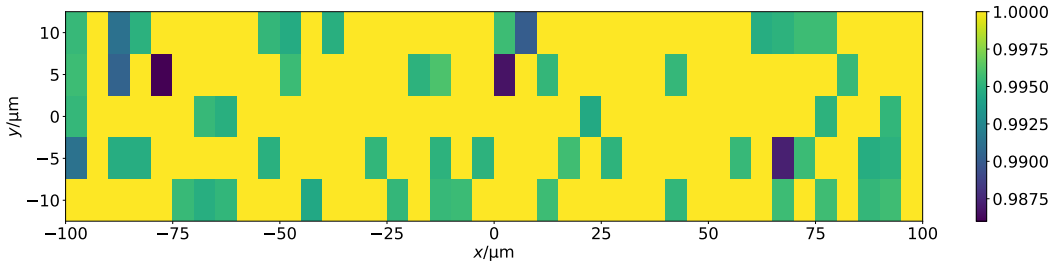

(A) Stitched

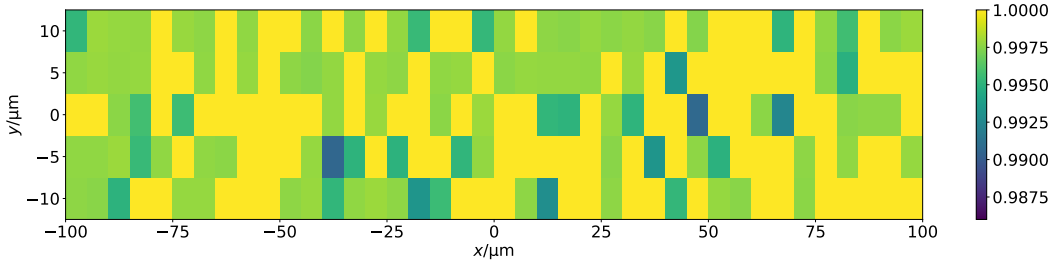

(B) Non-stitched

FIGURE 6.14: Measured efficiencies for 12° incidence for stitched (A) and non-stitched (B) pixels. No difference can be observed between the stitched and non-stitched pixels.

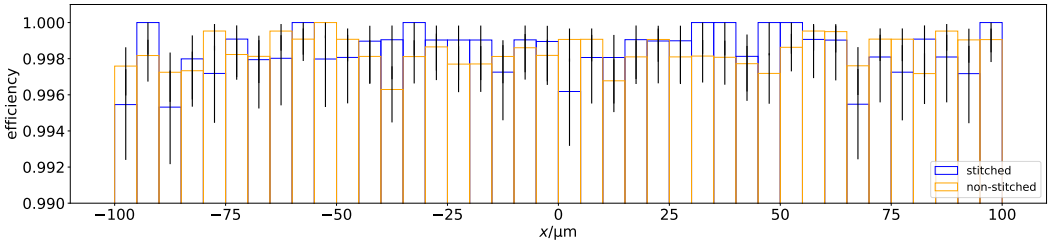

FIGURE 6.15: Measured efficiencies for 12° incidence for stitched and non-stitched pixels. The error bars represent the Clopper-Pearson confidence intervals for the efficiencies. No difference between the stitched and non-stitched pixels can be observed with in the statistical limits.

Chapter 7

Impact of the η-correction on the resolution of the sensor

Non-linear charge division results in a worse spatial resolution for two pixel clusters. The η-algorithm is a method for computing the cluster position which takes the non-linearities into account [38]. This should in principle be able to improve the spatial resolution for two pixel clusters. The impact of this correction has been studied for the resolution along the short pixel pitch of the passive CMOS sensors for angles between 0° and 12° and is presented in this chapter. Additionally, two different implementations of the η-correction were compared below.

7.1 Resolution

The resolution of the sensor can be measured by comparing the position of clusters on the sensor with the position of the associated, reconstructed track from the telescope. This is done for both the x- and y-directions independently. The usual way to compute the cluster position on the DUT is to use the charge weighted mean position:

$$x_{cluster} = \frac{\sum_i x_i Q_i}{\sum_i Q_i}, \tag{7.1}$$

where x_i are the positions and Q_i the collected charges of each pixel in the cluster. For each track, the difference between the cluster position on the sensor and the track position on the DUT is computed, which gives the residuals Δx:

$$\Delta x = x_{cluster} - x_{track}. \tag{7.2}$$

The standard deviation of the residual distribution contains the resolution of the sensor and the track resolution of the telescope:

$$\sigma^2_{\Delta x} = \sigma^2_{DUT} + \left(\frac{\sigma_{telescope}}{\cos\theta}\right)^2, \tag{7.3}$$

with θ being the incidence angle of the beam. This means that the sensor resolution can be computed as:

$$\sigma_{DUT} = \sqrt{\sigma^2_{\Delta x} - \left(\frac{\sigma_{telescope}}{\cos\theta}\right)^2} \tag{7.4}$$

Using a simulation for the track resolution of pixel beam telescopes [39] for the telescope setup depicted in Figure 5.2, the telescope resolution at the position of the

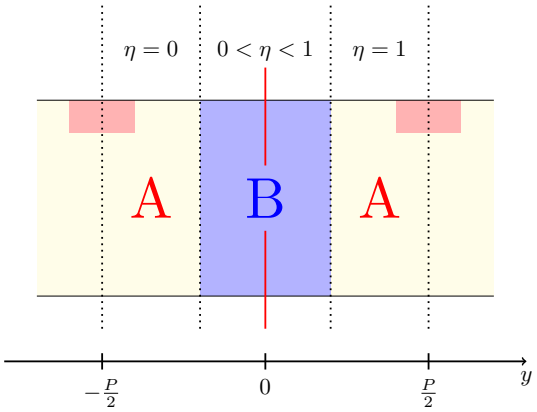

FIGURE 7.1: Definitions of regions A and B. The red line represents the boundary between two pixels. In region B charge division is effective. In region A only one pixel clusters will be registered. Figure adapted from [38].

DUT is found to be:

$$\sigma_{telescope} = 3.4\,\mu\text{m}. \tag{7.5}$$

7.2 The η-algorithm

For clusters with only one pixel Equation 7.1 implies that the cluster position always equals the center of the single pixel, which limits the resolution for one pixel clusters to effectively $\frac{y_{pitch}}{\sqrt{12}}$. For clusters with larger cluster sizes, charge division allows for a better spatial resolution. The amount of charge division is quantified by the η-variable:

$$\eta = \frac{Q_L}{Q_L + Q_R}, \tag{7.6}$$

where Q_L and Q_R are the charges collected by the left most and right most pixels of the cluster respectively. A value of $\eta = 0$ or $\eta = 1$ corresponds to one pixel clusters, any value between corresponds to two and more pixel clusters.

Charge division is non-linear in the pixels. The region where charge division is effective depends on the incidence angle of the particle and the diffusion of charges in the sensor [38]. For orthogonal incidence and a sensor thickness of 150 µm the size of the diffusion cloud is about 5 µm [40] (as can also be seen from Figure 6.1). This means that two pixel clusters will be concentrated in the regions close to the edges of the pixels. This corresponds to region B in Figure 7.1, whereas in region A only values of $\eta = 0$ and $\eta = 1$ will be registered.

The η-distribution for the measured passive CMOS sensor along the short pixel pitch of 25 µm is shown in Figure 7.2. The two large peaks at $\eta = 0$ and $\eta = 1$ correspond to the one pixel clusters. The region $0 < \eta < 1$ is filled by the clusters of size two and larger.

7.2.1 η-correction from the η-distribution

Computing the cluster position of two pixel clusters using Equation 7.1 will result in positions distributed across the whole cluster, which worsens the resolution. Since the hits are uniformly distributed across the sensor, the cluster position of two pixel

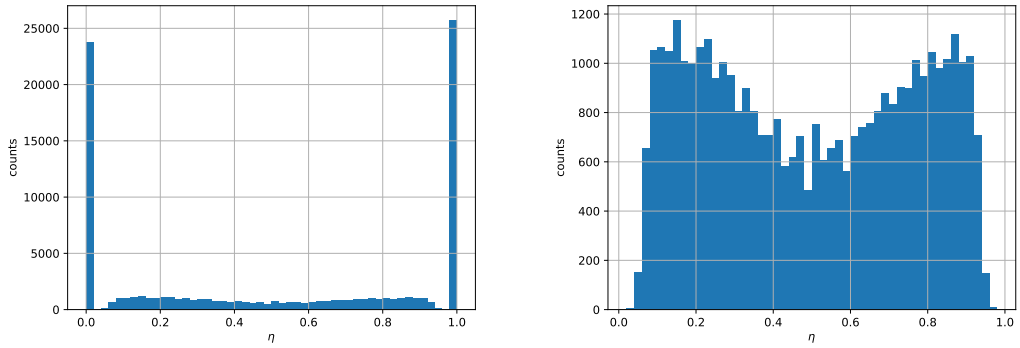

(A) Full η-distribution.

(B) η-distribution without $\eta = 0$ and $\eta = 1$.

FIGURE 7.2: Measured η-distribution for orthogonal incidence. Charge division is only effective for track close to the pixel edeges. The two peaks at $\eta = 0$ and $\eta = 1$ correspond to the one pixel clusters generated in the center of the pixel.

clusters can be calculated with respect to the center of the left pixel using the integral of the η-distribution [38]:

$$y_\eta = P\frac{\int_0^\eta \frac{dN}{d\eta'}d\eta'}{\int_0^1 \frac{dN}{d\eta'}d\eta'} = Pf(\eta), \tag{7.7}$$

where $\frac{dN}{d\eta'}$ is the differential η-distribution shown in Figure 7.2, and P is the pixel pitch. The function $f(\eta)$ was computed by integrating the histogram of the η-distribution for each incidence angle between 0° and 12°.

Figure 7.3 shows a comparison between the shape of the impact position reconstructed from the telescope tracks and the function $f(\eta)$ for two pixel clusters. Both follow the same shape, confirming that Equation 7.7 correctly reconstructs the cluster position of two pixel clusters.

This procedure does not require any track information and can be done without a beam telescope. The results of the η-correction are shown in section 7.3.

7.2.2 η-correction from telescope tracks

Another possiblity to implement the η-correction is using the cluster positions and reconstructed track positions from a testbeam telescope. As the η-correction only depends on the intrinsic properties of the sensor, the η-correction can then be reused for measurements without a telescope, as long as the properties do not change, for example due to radiation damage.

For all clusters with cluster size two, the mean telescope track position was computed as a function of the cluster position found with Equation 7.1. A plot of the mean telescope track positons is shown in Figure 7.4 for normal incidence. Then a polynomial function was fitted to the data points. The degree n of the polynomial fit is determined by using a F-test. After an initial fit with $n = 1$, the data is refitted with $n_{test} = n + 1$ and the χ^2 is computed for both fits. Then the F-value can be

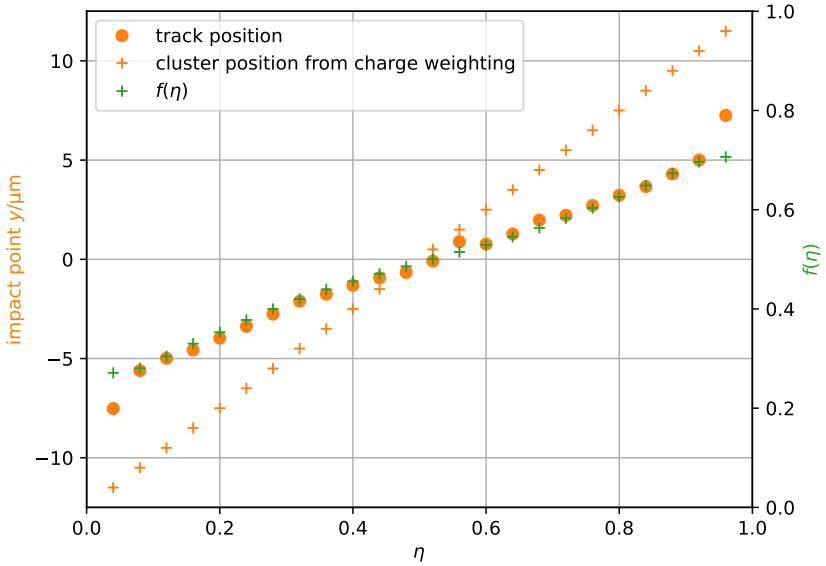

FIGURE 7.3: Comparison between the reconstructed impact positions from the telescope (orange dots) and $f(\eta)$ from Equation 7.7 (green plusses) for two pixel cluster. Both distributions show the same shape, confirming that the η-alogrithm correctly reconstructs the cluster position for two pixel clusters. The orange plusses depict the reconstructed cluster positions from simple charge weighting (Equation 7.1) showing that this method is not able to correctly reconstruct the cluster position.

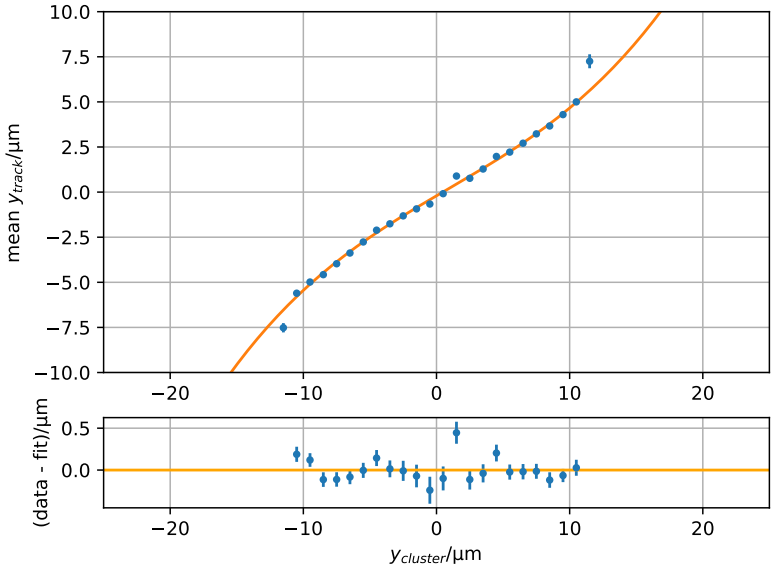

FIGURE 7.4: Mean track position as a function of the cluster position computed with Equation 7.1 for orthogonal incidence. The data was fit with a third order polynomial (orange line), which gives the η-correction.

computed as:

$$F = \frac{\left(\frac{\chi^2 - \chi^2_{test}}{n_{test} - n}\right)}{\left(\frac{\chi^2_{test}}{n_{tot} - n_{test}}\right)}, \tag{7.8}$$

where n_{tot} is the total number of degrees of freedom in the fit. If n_{test} does not provide a significantly better fit, F will follow an F-distribution with numbers of degrees of freedom $n_{tot} - n$ and $n_{tot} - n_{test}$. For each step, the p-value for the measured value of F is calculated. If $p < 0.05$, the fit with degree n_{test} is accepted and the procedure is repeated with a new $n = n_{test}$. If $p > 0.05$, both fits describe the data similarly well and the fit with n degrees is accepeted. The resultant third order polynomial fit for orthogonal incidence is shown in Figure 7.4.

The fit gives a function $g(y_{cluster})$ which gives the mean reconstructed track position, as a function of the cluster position computed with Equation 7.1. The η-correction is applied by directly computing the corrected position from this function for each cluster:

$$y_\eta = g(y_{cluster}). \tag{7.9}$$

This procedure is repeated for incidence angles between 0° and 12°. The results of this correction are shown in the next section.

7.3 Results

The residual distributions for two pixel clusters along the short pixel pitch (with and without η-corrections) for orthogonal incidence are shown in Figure 7.5. All three distributions were fitted with a Student's t-distribution. A significant improvement

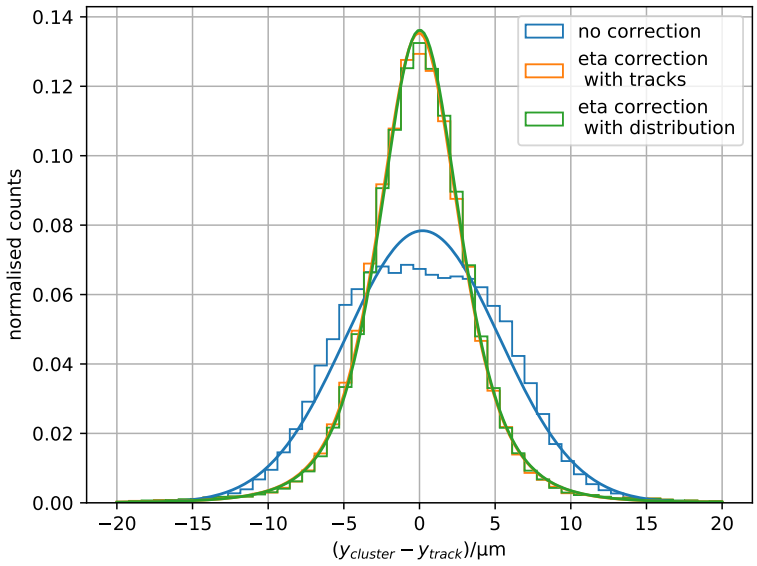

FIGURE 7.5: Residual distributions for two pixel clusters along the short pixel pitch for orthogonal incidence. All three distributions were fitted with a Student's t-distribution. The η-correction reduces the resolution significantly. Both procedures for the η-correction show equivalent results.

of the resolution can be seen for the η-corrected distributions. Without any correction a DUT resolution of 3.8 µm is achieved for two pixel clusters. With the η-corrections applied, the resolution decreases to 1.9 µm for both procedures (tracks and distribution). The mean residuals as a function η are shown in Figure 7.6 for orthogonal incidence. Without any correction, the residuals are negatively biased for $\eta < 0.5$ and positively biased for $\eta > 0.5$ due to the non-linear charge division inside the pixels. With the η-correction, the residuals become unbiased with respect to η. Both procedures for the η-correction show the same results and can therefore be assumed as equivalent.

The DUT resolution for two pixel clusters along the short pixel pitch for angles between 0° and 12° is shown in Figure 7.7. The two different procedures for the η-correction again show equivalent results. The η-correction significantly improves the DUT resolution by about a factor of two for small angles. At about 4° a minimal resolution for two pixel-clusters of 1.0 µm is achieved. For larger angles the effect of the η-resolution decreases due to the inclination of the track generating more two pixel clusters. This makes the charge division more linear for larger angles, diminishing the effects of the η-correction. At an angle of 9° the non-corrected and η-corrected data give the same resolution. This is in accordance with the expectation that for $\theta = \arctan(25\,\mu m/150\,\mu m) \approx 9.5°$ all tracks will hit two pixels and charge division will almost be fully linear.

As both the method using the integral of the distribution does not rely on a testbeam measurement with a beam telescope and both methods deliver similar results, the usage of the distribution seems more beneficial over the usage of the tracks. In this way, the η-correction can be continuously adapted with new data, even during the measurement in the final experiments. In this way, the correction can be adapted to

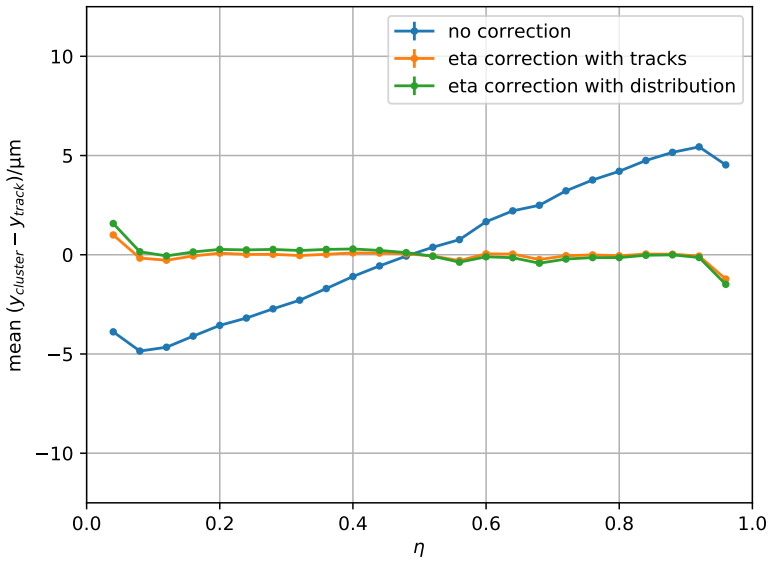

FIGURE 7.6: Mean residuals as a function of η. The uncorrected residuals are negtively biased for $\eta < 0.5$ and positively biased for $\eta > 0.5$ due to the non-linear charge division in the pixels. The η-correction removes this dependence of the residuals on η. Both procedures for the η-correction show equivalent results.

changing sensor properties for example due to radiation damage.

7.4 Summary

Simple charge weighting (Equation 7.1) does not lead to correct reconstruction of the cluster position for two pixel clusters. This leads to a loss in spatial resolution on the sensor. The main reason for this is non-linear charge division among the pixels. The η-correction uses the information on the non-linearity of the charge division in order to give a better reconstruction of the cluster position of two pixel clusters and thus a better spatial resolution. The η-correction has been implemented using two different methods and its impact was checked on data from a passive CMOS sensor with pixel pitch 100 µm × 25 µm for incidence angles between 0° and 12°. One method integrates the η-distribution to calculate the correction (section 7.2.1), the second method uses the track information from a beam telescope (section 7.2.2). Both methods show the same results and improve the two pixel cluster resolution along the 25 µm pixel pitch by a factor of two for angles bewlow 4°. At this angle, a minimal resolution of 1.0 µm is reached. For angles larger than 9°, no improvement of the resolution is seen as expected for the given pixel dimensions, since all track will hit two pixels and charge division will be almost fully linear.

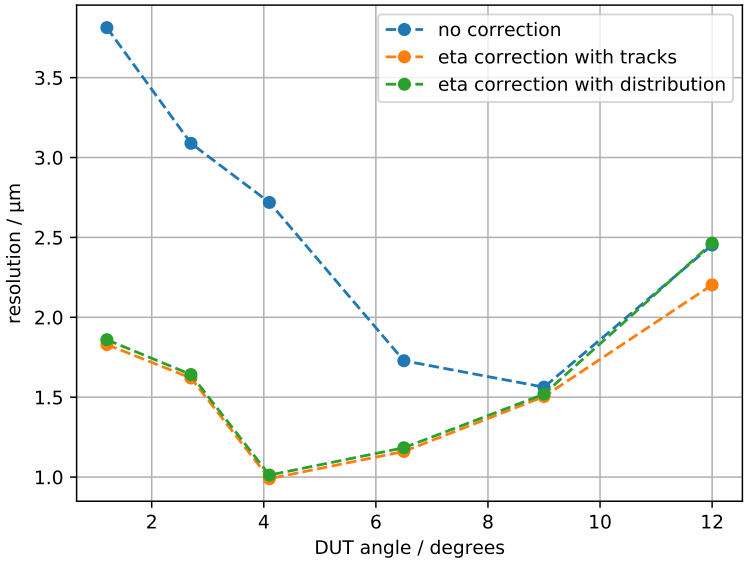

FIGURE 7.7: DUT residuals for different angles. The η-correction significantly improves the resolution for small angles. For larger angles the effect decreases due to the inclination of the tracks making two pixel clusters more probable. For an angle 9° no improvement is left as the charge divison is almost fully linear for this angle.

Chapter 8

Conclusion

In this master thesis the impact of stitching on the performance of an unirradiated passive CMOS pixel sensors for the Phase-II upgrade of the CMS detector and the effects of the η-correction on the resolution of two pixel clusters have been investigated.

The two pixel columns adjacent to the stitching line were compared to columns without a stitching line between them. Due to a problem of the charge calibration of the readout chip, only columns close to the columns with stitching were used for the comparison. The stitched and non-stitched columns were compared in the measured cluster size, charge collection, charge diffusion and detection efficiency for two different beam incidence angles of 0° and 12° along the short pixel pitch. The stitched columns were checked for differences compared to the non-stitched columns and for the requirements set for the Phase-II upgrade of the CMS pixel detector. No differences between the stitched and non-stitched pixels were found for the measured quantites. All quantities showed the expected in-pixel distributions for both incident angles. Both stitched and non-stitched pixels reach the required detection efficiency of 99 %. The results show that the usage of stitching in the production of passive CMOS sensors does not influence the perfomance of these sensors. The usage of stitching and CMOS processes allows for the production of larger area sensors at lower costs and with more design possibilities, rendering them as beneficial in high energy physics, especially for future small-pixel designs.

Two different procedures of implementing the η-correction have been presented. One uses the integral of the η-distribution, the second uses the track information from the telescope from the testbeam measurement. Both procedures show the same results. The two pixel cluster resolution along the short pixel pitch is significantly improved by a factor of about two for angles below 4°, reaching a minimal resolution of 1.0 µm. No improvement on the resolution is seen anymore for an angle of 9°, as expected for the dimensions of the pixels. The usage of the integrated η-distribution seems more beneficial as it can be used and adapted independently from a beam telescope.

Bibliography

[1] O. Aberle et al., *High-Luminosity Large Hadron Collider (HL-LHC): Technical design report*, CERN Yellow Reports: Monographs (CERN, Geneva, 2020), http://cds.cern.ch/record/2749422.

[2] D. Contardo et al., *Technical Proposal for the Phase-II Upgrade of the CMS Detector*, tech. rep. (Geneva, June 2015), https://cds.cern.ch/record/2020886.

[3] CMS Collaboration, *The Phase-2 Upgrade of the CMS Tracker*, tech. rep. (CERN, Geneva, June 2017), https://cds.cern.ch/record/2272264.

[4] S. Fartoukh et al., *LHC Configuration and Operational Scenario for Run 3*, tech. rep. (CERN, Geneva, Nov. 2021), https://cds.cern.ch/record/2790409.

[5] M. Benedikt et al., *LHC Design Report*, CERN Yellow Reports: Monographs (CERN, Geneva, 2004), http://cds.cern.ch/record/823808.

[6] G. Aad et al. (ATLAS Collaboration), "The ATLAS Experiment at the CERN Large Hadron Collider", JINST **3**, Also published by CERN Geneva in 2010, S08003. 437 p (2008), https://cds.cern.ch/record/1129811.

[7] S. Chatrchyan et al. (CMS Collaboration), "The CMS experiment at the CERN LHC. The Compact Muon Solenoid experiment", JINST **3**, Also published by CERN Geneva in 2010, S08004. 361 p (2008), https://cds.cern.ch/record/1129810.

[8] A. A. Alves et al. (LHCb Collaboration), "The LHCb Detector at the LHC", JINST **3**, Also published by CERN Geneva in 2010, S08005 (2008), https://cds.cern.ch/record/1129809.

[9] K. Aamodt et al. (ALICE Collaboration), "The ALICE experiment at the CERN LHC. A Large Ion Collider Experiment", JINST **3**, Also published by CERN Geneva in 2010, S08002. 259 p (2008), https://cds.cern.ch/record/1129812.

[10] G. Aad et al. (ATLAS collaboration), "Observation of a new particle in the search for the Standard Model Higgs boson with the ATLAS detector at the LHC", Physics Letters B **716**, 1–29 (2012), https://www.sciencedirect.com/science/article/pii/S037026931200857X.

[11] S. Chatrchyan et al. (CMS collaboration), "Observation of a new boson at a mass of 125 GeV with the CMS experiment at the LHC", Physics Letters B **716**, 30–61 (2012), https://www.sciencedirect.com/science/article/pii/S0370269312008581.

[12] R. Aaij et al. (LHCb collaboration), *Test of lepton universality in beauty-quark decays*, 2021.

[13] M. Vretenar et al., *Linac4 design report*, Vol. 6, CERN Yellow Reports: Monographs (CERN, Geneva, 2020), https://cds.cern.ch/record/2736208.

[14] R. Vanden Broeck, "THE CERN ACCELERATOR COMPLEX. Complexe des accélérateurs du CERN", Sept. 2019, https://cds.cern.ch/record/2693837.

[15] ATLAS collaboration, *ATLAS public plots website*, https://twiki.cern.ch/twiki/bin/view/AtlasPublic/LuminosityPublicResultsRun2#Multiple_Year_Collision_Plots (visited on Mar. 9, 2022).

[16] CMS collaboration, *CMS public plots website*, https://twiki.cern.ch/twiki/bin/view/CMSPublic/LumiPublicResults#Multi_year_plots (visited on Mar. 9, 2022).

[17] *Run 3 luminosity targets*, Mar. 2022, https://lhc-commissioning.web.cern.ch/performance/Run-3-targets.htm.

[18] W. Adam et al., "The CMS phase-1 pixel detector upgrade", Journal of Instrumentation **16**, P02027–P02027 (2021), https://doi.org/10.1088/1748-0221/16/02/p02027.

[19] "Detector Drawings", CMS Collection., Mar. 2012, https://cds.cern.ch/record/1433717.

[20] S. Orfanelli, "The phase 2 upgrade of the cms inner tracker", Nuclear Instruments and Methods in Physics Research Section A: Accelerators, Spectrometers, Detectors and Associated Equipment **980**, 164396 (2020), https://www.sciencedirect.com/science/article/pii/S0168900220307932.

[21] C. W. Fabjan, H. Schopper, and S. Myers, *Particle physics reference library* (Springer, Cham, 2020), https://cds.cern.ch/record/2702370.

[22] P. A. Zyla et al. (Particle Data Group), "Review of Particle Physics, 2020-2021. RPP", PTEP **2020**, 083C01. 2093 p (2020), https://cds.cern.ch/record/2729066.

[23] J. H. Hubbell and S. M. Seltzer, *Tables of X-ray mass attenuation coefficients and mass energy-absorption coefficients 1 keV to 20 MeV for elements Z=1 to 92 and 48 additional substances of dosimetric interest*, tech. rep. (May 1995), http://cds.cern.ch/record/353989.

[24] L. Rossi et al., *Pixel detectors: from fundamentals to applications*, Particle acceleration and detection (Springer, Berlin, 2006), http://cds.cern.ch/record/976471.

[25] PhysicsOpenLab, *Charge sensitive preamplifier*, Sept. 2017, https://physicsopenlab.org/2017/09/27/charge-sensitive-preamplifier/.

[26] G. Hall, "Recent progress in front end ASICs for high-energy physics", Nucl. Instrum. Methods Phys. Res., A **541**, 248–258 (2005), http://cds.cern.ch/record/908846.

[27] F. Hartmann, *Evolution of Silicon Sensor Technology in Particle Physics* (Springer, Cham, 2017), https://doi.org/10.1007/978-3-319-64436-3.

[28] Y. Dieter et al., "Radiation tolerant, thin, passive CMOS sensors read out with the RD53a chip", Nuclear Instruments and Methods in Physics Research Section A: Accelerators, Spectrometers, Detectors and Associated Equipment **1015**, 165771 (2021), https://doi.org/10.1016%2Fj.nima.2021.165771.

[29] J. (Chistiansen and M. (Garcia-Sciveres, *RD Collaboration Proposal: Development of pixel readout integrated circuits for extreme rate and radiation*, tech. rep., The authors are editors on behalf of the participating institutes. the participating institutes are listed in the proposal (CERN, Geneva, June 2013), https://cds.cern.ch/record/1553467.

[30] M. Garcia-Sciveres (RD53 Collaboration), *RD53A Integrated Circuit Specifications*, tech. rep. (CERN, Geneva, Dec. 2015), https://cds.cern.ch/record/2113263.

[31] M. Garcia-Sciveres (RD53 Collaboration), *The RD53A Integrated Circuit*, tech. rep. (CERN, Geneva, Oct. 2017), https://cds.cern.ch/record/2287593.

[32] *CMS Tracker Phase2 Acquisition & Control Framework*, [Online], 2021, https://gitlab.cern.ch/cms_tk_ph2/Ph2_ACF.

[33] L. Gaioni, *Linear Analog Front-end Guidelines and Recommendations* (July 2018), https://twiki.cern.ch/twiki/pub/RD53/RD53ATesting/LIN_AFE_guidelines.pdf.

[34] I. Rubinskiy, "An EUDET/AIDA Pixel Beam Telescope for Detector Development", Physics Procedia **37**, Proceedings of the 2nd International Conference on Technology and Instrumentation in Particle Physics (TIPP 2011), 923–931 (2012), https://www.sciencedirect.com/science/article/pii/S1875389212017889.

[35]P. Ahlburg et al., "EUDAQ—a data acquisition software framework for common beam telescopes", Journal of Instrumentation **15**, P01038–P01038 (2020), https://doi.org/10.1088/2F1748-0221/2F15/2F01/2Fp01038.

[36]D. Dannheim et al., "Corryvreckan: a modular 4D track reconstruction and analysis software for test beam data", Journal of Instrumentation **16**, P03008 (2021), https://doi.org/10.1088/1748-0221/16/03/p03008.

[37]C. J. CLOPPER and E. S. PEARSON, "THE USE OF CONFIDENCE OR FIDUCIAL LIMITS ILLUSTRATED IN THE CASE OF THE BINOMIAL", Biometrika **26**, 404–413 (1934), https://doi.org/10.1093/biomet/26.4.404.

[38]R. Turchetta, "Spatial resolution of silicon microstrip detectors", Nuclear Instruments and Methods in Physics Research Section A: Accelerators, Spectrometers, Detectors and Associated Equipment **335**, 44–58 (1993), https://www.sciencedirect.com/science/article/pii/016890029390255G.

[39]S. Spannagel and H. Jansen, *Gbl track resolution calculator v2.0*, version v2.0, Apr. 2016, https://doi.org/10.5281/zenodo.48795.

[40]E. J. Schioppa et al., "Study of charge diffusion in a silicon detector using an energy sensitive pixel readout chip", IEEE Transactions on Nuclear Science **62**, 2349–2359 (2015).

[41]Izaak Neutelings, *CMS coordinate system*, https://tikz.net/axis3d_cms/ (visited on Apr. 11, 2022).

Appendix A

CMS coordinate system

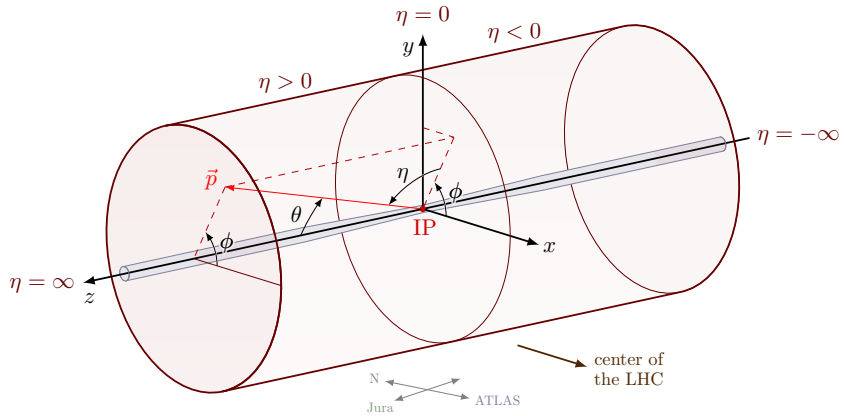

FIGURE A.1: Sketch of the coordinate system adopted by the CMS experiment. Figure reproduced from [41].

The coordinate system adopted by CMS is a right-handed coordinate system with the origin centered at the nominal collision point inside the experiment. A sketch of the coordinate system is shown in Figure A.1 The x-axis is pointing radially inward towards the the center of the LHC, the y-axis is pointing vertically upward and the z-axis points along the beam direction. The cooridnate r is the radial coordinate in the $x-y$ plane and the azimuthal angle ϕ is the angle in this plane measured from the x-axis. The polar angle θ is measured from the z-axis. Often the pseudorapidity $\eta = -\ln\tan(\theta/2)$ is given instead of θ.